The Simulation of Three-Dimensional Convective Storm Dynamics

JOSEPH B. KLEMP

National Center for Atmospheric Research[1], Boulder, Colo. 80307

ROBERT B. WILHELMSON

University of Illinois, Urbana 61801

(Manuscript received 22 September 1977, in final form 21 February 1978)

ABSTRACT

A new three-dimensional cloud model has been developed for investigating the dynamic character of convective storms. This model solves the compressible equations of motion using a splitting procedure which provides numerical efficiency by treating the sound wave modes separately. For the subgrid turbulence processes, a time-dependent turbulence energy equation is solved which depends on local buoyancy, shear and dissipation. First-order closure is applied to nearly conservative variables with eddy coefficients based on the computed turbulence energy. Open lateral boundaries are incorporated in the model that respond to internal forcing and permit gravity waves to propagate out of the integration domain with little apparent reflection. Microphysical processes are included in the model using a Kessler-type parameterization. Simulations conducted for an unsheared environment reveal that the updraft temperatures follow a moist adiabatic lapse rate and that the convection is dissipated by water loading of the updraft. The influence of a one-directional shear on the storm development is also investigated. A simulation with a veering and backing wind profile exhibits interesting features which include a double vortex circulation, cell splitting and secondary cell formation.

1. Introduction

In recent years, the detailed three-dimensional structure of convective storms has been observationally well documented. Schematic models based on these observations have been proposed (e.g., Fankhauser, 1971; Browning and Foote, 1976), and analyses of multiple-Doppler observations are now revealing the internal velocity structure within precipitating clouds (Ray, *et al.*, 1975; Ray, 1976; Brandes, 1977; Miller, 1975; Kropfli and Miller, 1976; Lhermitte and Gilet, 1975). To further increase our understanding of cloud structures and their relationship to environmental conditions and microphysical processes many numerical models have also been developed. However, only recently have three-dimensional simulations been seriously attempted, primarily because of computational constraints.

Three-dimensional simulations are necessary for studying the relationship between shearing and veering environmental winds and such features as rotation within and orientation of updrafts and downdrafts, cloud movement relative to the mean wind direction and flow of environmental wind around a cloud. For example, Orville and Kopp (1977) found it necessary to reduce environmental winds to 20% of the observed values in their two-dimensional model in order to simulate the Fleming supercell storm which occurred on 21 June 1972 in the NHRE project area and which has been documented by Browning and Foote (1976). Frequently in two-dimensional (and often in three-dimensional) models rain falls within the updraft and the downdraft that eventually develops due to water loading and subcloud evaporation cuts off the primary low-level supply of moisture (e.g., Wilhelmson, 1974). Despite some success by Orville and Kopp (1977), Takeda (1971), Hane (1973) and Schlesinger (1973a,b) in modeling storm features with two-dimensional models there still remain many features such as those mentioned above which these models cannot faithfully represent. Further, it is not clear under what conditions the ability to represent subgrid-scale motions in three dimensions will be important to cloud development and structure. For example, Kraichnan (1976) has discussed the different implications of eddy viscosity assumptions in two and three dimensions including the tendency for transfer of kinetic energy to larger scales in two dimensions and to smaller scales in three dimensions.

Three-dimensional modeling currently requires sacrifices in the representation of physical processes and in the scales of resolution which must be made through

[1] The National Center for Atmospheric Research is sponsored by the National Science Foundation.

0022-4928/78/1070-1096$13.50

careful consideration of one's modeling goals. It is not feasible, for example, to model storm evolution with a grid that lies well within the inertial subrange, with a domain three or four times the storm size, and with a detailed representation of microphysical interactions. Resolution within the inertial subrange is desirable because the statistical nature of transport processes within this subrange is basically understood (e.g., Lilly, 1967). These statistics justify the use of turbulence parameterizations which are much simpler than those using the full second-moment turbulence equations (Deardorff, 1973) which are presently too complex for use in a three-dimensional cloud model. At the same time, having a large domain relative to the storm is desirable in order to capture storm interaction with its environment. For example, Hoxit *et al.* (1976) suggest that a midlatitude storm can interact with the environment to form a mesolow 25–100 km downwind of the existing storm, inducing low-level moisture convergence which is favorable for continued storm development. Finally, a detailed representation of the microphysics would be desirable because the timing and location of precipitation can have a significant effect on the dynamics.

The three-dimensional cloud and storm modelers that have reported in the literature have made sacrifices in each of these areas. The main emphasis of their research has been on the basic development of three-dimensional models and on their use to simulate cloud structure, intensity and movement. Steiner (1973) utilized a shallow convection model for both dry and nonprecipitating simulations. Schlesinger (1975) reported some preliminary results from a deep and nonprecipitating convection mode. Wilhelmson (1974), Pastushkov (1975), Miller and Pearce (1974) and Moncrieff and Miller (1976) have simulated deep precipitating convection in which the microphysics has been highly parameterized. A unique feature of the Miller model is that the vertical coordinate is pressure while in the other models it is height. For computational reasons Steiner, Pastushkov and Wilhelmson implemented their models assuming symmetry across a vertical plane and thus were not able to vary the direction of the environmental wind with height.

Schlesinger (1975) and Wilhelmson (1974) have pointed out the presence of vortex couplets within the updraft for cases involving one-directional shear. However, it is difficult to determine what path an air parcel takes as it rises within this couplet, what the origin of the couplet is and, in Wilhelmson's precipitating case, what relationship the couplet has to Doppler observations. Answers are complicated by the nonsteady nature of the simulated clouds and the corresponding difficulty in choosing an appropriate propagation speed. Wilhelmson notes that at mid-cloud levels wind features reminiscent of flow about an obstacle are present, i.e., deceleration of approaching air and acceleration of the air as it passes around the updraft. Wilhelmson also documents the depletion of low-level moisture that occurs when moisture is not replenished through the boundaries.

Moncrieff and Miller (1976) used theory and numerical simulations to discuss the maintenance of tropical cumulonimbi that tend to propagate faster than the wind at any level in which they are embedded. They argue that under certain conditions a density current due to a diverging downdraft near the ground propagates at the same speed as the cloud and the net result is a convergent region beneath the updraft. This occurs despite the fact that rain falls out downshear of the updraft. They also argue that simplified cloud microphysical and subgrid parameterizations appear to be adequate for representing the dynamic character of tropical cumulonimbus.

The main purpose of this paper is to present the development of a new three-dimensional model for continuing the study of the dynamic character of convective clouds and storms. The previously mentioned investigations only begin to answer the many questions which arise with regard to cloud structure and dynamics. For example, what environmental factors have most effect on cloud and storm longevity, propagation and intensity; how do clouds evolve into severe storms; and what are typical net transports of momentum and heat by storms? Answers to these questions probably vary depending on the kind of storm being investigated, e.g., supercells, multicells, squall lines, etc. We have taken considerable care to formulate and implement a new model that can be used to help answer questions of this nature.

In Section 2a we present the dynamical model based on the compressible equations of motion, while in Section 2b we describe the microphysical parameterization. The subgrid turbulence parameterization, discussed in Section 2c, utilizes mixing coefficients obtained through the solution of a subgrid kinetic energy equation with closure applied to nearly conservative variables. Boundary conditions are presented in Section 2d. They appear to be well posed and are designed to allow the dominant gravity wave modes to propagate out through the lateral boundaries without significant reflection.

Sections 3a–3d deal with the finite-difference representation of equations in the corresponding parts of Section 2. Here a computationally efficient technique for integration of the compressible equations is described. Efficiency is achieved by solving for the sound wave terms separately using a smaller time step. Sections 3e and 3f include information on numerical smoothing used and on code implementation, respectively. Tests performed using the model are presented in Section 4. These include testing the ability of the model to represent parcel ascent, determining the effects of the subgrid parameterization, documenting the significance of the open lateral boundary conditions in both two and three dimensions, and studying two-dimensional

model sensitivity to the specification of boundary conditions and to variations within the microphysical representation. Finally, in Section 5 the results of a three-dimensional simulation initiated with a veering and backing wind are discussed in some detail.

2. Model equations

In developing the three-dimensional cloud model, strong emphasis has been placed on providing a sound dynamical framework for the system with initially rather simple microphysics. This approach seems justified in that accurate dynamics are a necessary prerequisite for studying storm circulations. Detailed microphysics can then be accommodated as procedures are developed for simplifying the more sophisticated parameterizations.

The equations of motion which govern cloud-scale motion are compressible and thus permit the propagation of both gravity and sound wave modes. Although sound waves are not important in thermal convection, their presence can place severe restrictions on the time step in numerical integrations because of their high propagation speed. For this reason most cloud modelers use an anelastic system of equations in which sound waves have been removed by eliminating certain terms in the compressible equations. The anelastic system was proposed and analyzed by Ogura and Charney (1962) and Ogura and Phillips (1962). To our knowledge only Hill (1974) and Cotton (personal communications) have used the compressible equations in cloud modeling. The time step required for their numerical integrations is considerably smaller than that required for corresponding anelastic integrations because numerical stability depends on the speed of sound. Miller (1974) and Miller and Pearce (1974) also eliminated sound waves from their model, but fast moving external gravity waves remained to limit the time step. Moncrieff and Miller (1976) removed the surface gravity waves from the model, allowing larger time steps.

The compressible equations, however, have certain advantages over the anelastic equations, particularly in three dimensions. These will be discussed in Section 2a. Consequently, our model utilizes the compressible equations along with procedures to significantly improve the computational efficiency.

The current version of the model contains nine prognostic equations. They include the three momentum equations, the pressure and thermodynamic equations, three moisture and water equations, and a subgrid kinetic energy equation. The equations are specified in the Cartesian coordinate system and will be described in Sections 2a–2c.

a. The dynamic framework

Derivatives of the momentum and pressure equations require use of the moist equation of state which is commonly written in the form

$$p=\rho R_d T(1+0.61q_v), \tag{2.1}$$

where p is the pressure, ρ the density of moist air, R_d the gas constant for dry air, T the temperature and q_v the mixing ratio of water vapor. Eq. (2.1) can be rewritten in terms of nondimensional pressure Π in the form

$$\Pi=\left(\frac{p}{p_0}\right)^{R_d/c_p}=\left(\frac{R_d}{p_0}\rho\theta_v\right)^{R_d/c_v}. \tag{2.2}$$

Here p_0 is the base state pressure at the ground and θ_v the virtual potential temperature defined by

$$\theta_v=\theta(1+0.61q_v). \tag{2.3}$$

The potential temperature θ is then simply related to Π by $\theta=T/\Pi$.

The momentum equations are derived from the Navier–Stokes equations with the aid of (2.1). The results can be expressed in tensor form as

$$\frac{du_i}{dt}+c_p\bar{\theta}_v\frac{\partial\pi}{\partial x_i}=\delta_{i3}g\left[\frac{\theta}{\bar{\theta}}-1+0.61(q_v-\bar{q}_v)-q_c-q_r\right]$$
$$-\epsilon_{ij3}fu_i+D_{u_i}. \tag{2.4}$$

The u_i ($i=1, 2, 3$) are the velocities u, v, w, respectively, π is the deviation of pressure from the initial unperturbed state $\bar{\Pi}$, and q_c and q_r are the mixing ratios of cloud drops and rainwater, respectively. These equations include the Coriolis force, with f being the Coriolis parameter. Bars over individual variables refer to the initial undisturbed state which is a function of z only. The operator d/dt denotes the substantial derivative given by

$$\frac{d}{dt}\equiv\frac{\partial}{\partial t}+u_j\frac{\partial}{\partial x_j}.$$

Terms denoted by D_{u_i} represent the subgrid turbulent mixing and are defined in Section 2c. The buoyancy term in (2.4) arises through linearization of the pressure term and use of (2.1), (2.2), (2.3) and the hydrostatic equation $\bar{\Pi}_z=-g/(c_p\bar{\theta}_v)$.

The prognostic equations for θ, q_v, q_c and q_r can all be written in the form

$$\frac{d\phi}{dt}=M_\phi+D_\phi, \tag{2.5}$$

where M_ϕ refers to microphysical terms described in 2b and D_ϕ to turbulence terms defined in 2c.

The pressure equation is derived by taking the substantial derivative of (2.2) and using the compressible continuity equation

$$\frac{\partial\rho}{\partial t}+\frac{\partial}{\partial x_j}(\rho u_j)=0 \tag{2.6}$$

to eliminate $d\rho/dt$ and the thermodynamic equation to remove $d\theta/dt$. The resulting equation is

$$\frac{\partial \pi}{\partial t}+\frac{\bar{c}^2}{c_p\bar{\rho}\bar{\theta}_v^2}\frac{\partial}{\partial x_j}(\bar{\rho}\bar{\theta}_v u_j)=f_\pi, \tag{2.7a}$$

$$f_\pi=-u_j\frac{\partial \pi}{\partial x_j}+\frac{R_d\pi}{c_v}\frac{\partial u_j}{\partial x_j}+\frac{c^2}{c_p\theta_v^2}\frac{d\theta_v}{dt}+D_\pi, \tag{2.7b}$$

where c is the speed of sound given by $c^2=c_pR_d\Pi\theta_v/c_v$. This equation is similar to the one used by Tapp and White (1976) in their nonhydrostatic mesoscale model.

The anelastic continuity equation $\partial\bar{\rho}u_i/\partial x_i=0$ can be derived using (2.7) and scale analysis similar to that carried out by Ogura and Phillips (1962). This analysis suggests that only the second term in (2.7a) is physically important in describing convection. Since the anelastic approximation eliminates the prognostic nature of the equation, one must then solve an elliptic equation derived from the momentum and continuity equations which has the form (e.g., see Wilhelmson, 1974)

$$\frac{\partial^2}{\partial x_j^2}(\bar{\rho}\bar{\theta}_v\pi)=\text{source terms}. \tag{2.8}$$

Our decision to utilize the compressible equation (2.7a) rather than the anelastic equation (2.8) is based primarily on the computational simplicity and flexibility of using a fully prognostic system of equations. The numerical code then remains a set of explicit prognostic equations and alterations involving such things as stretched or nested grids, higher order finite-difference schemes and surface terrain, and boundary conditions can be incorporated into the numerical model without complicating the solution procedure. By special handling of the sound wave terms as described in the next section, the compressible equations can be solved nearly as efficiently as the anelastic system in which the Poisson equation has constant coefficients. With nonconstant coefficients (produced by such features as a stretched mesh or coordinate transformation) more general algorithms or iterative techniques are required which can make solution of the anelastic system more time consuming.

The terms contained in f_π in (2.7b) appear to have little influence on processes which are of physical interest in the cloud model. Derivation of the linear dispersion relation reveals that these terms have a very small influence on both sound and gravity wave modes. [Details will be discussed by Klemp (1978).] Since in the model the continuity equation is only used in deriving the pressure equation, simplification of (2.7a) is comparable to including a small source term in (2.6). Thus eliminating f_π in (2.7a) can allow small amounts of mass to be added to or removed from the domain which in turn affects the mean level of the pressure. This effect is similar to that occurring in the anelastic system where nonuniqueness of the Poisson solution requires an arbitrary specification of the mean pressure. Thus f_π is only important for uniqueness by allowing the mean pressure in the domain to be correctly represented. However, in the present model formulation a unique pressure is not required since only derivatives of π are needed. Even including f_π, computing a unique pressure field may not be feasible since with open lateral boundaries the mean pressure is sensitive to the net fluxes of mass and heat through the boundaries. Whether these fluxes are specified or computed, there is no unique way to determine what they would be if the artificial lateral boundaries were not present.

The cloud model is currently designed so that f_π can be either included or omitted in the computations. Including f_π requires one more storage array and causes only a small increase in the computation time. Simulations presented in this paper have been computed both ways and the differences are negligible except that the pressure fields differ by a constant which ranges up to a maximum of about 0.5 mb.

b. Microphysical parameterization

The microphysical processes of condensation and coalescence are represented by M_ϕ in (2.5) and are given by

$$M_\theta=-\gamma\left(\frac{dq_{vs}}{dt}+E_r\right), \tag{2.9a}$$

$$M_{q_v}=\frac{dq_{vs}}{dt}+E_r, \tag{2.9b}$$

$$M_{q_c}=-\frac{dq_{vs}}{dt}-A_r-C_r, \tag{2.9c}$$

$$M_{q_r}=-\frac{1}{\bar{\rho}}\frac{\partial}{\partial z}(\bar{\rho}Vq_r)-E_r+A_r+C_r. \tag{2.9d}$$

Here $\gamma=L/(c_p\bar{\Pi})$, L is the latent heat of vaporization, q_{vs} represents the saturation mixing ratio, and dq_{vs}/dt refers to the rate of condensation or evaporation of cloud water q_c. The terms A_r, C_r and E_r represent the rates of autoconversion, collection and evaporation of rain, respectively, and V is the terminal velocity of the rainwater.

Condensation and evaporation represented by the dq_{vs}/dt term are governed by the thermodynamic equation

$$\frac{d\theta}{dt}+\gamma\frac{dq_v}{dt}=D_\theta+\gamma D_{q_v}, \tag{2.10}$$

which is obtained by summing the θ equation with γ

times the q_v equation. Das (1969) argued that the left-hand side of (2.10) provides a good approximation to the standard expression for the water saturation adiabat given by Saunders (1957). Wilhelmson (1977) has also demonstrated that, for deep convection, Eq. (2.10) is a better approximation than conservation of equivalent potential temperature $\theta_e=\theta+\gamma q_v$. (The only difference between the two arises from the z dependence of γ.) To determine the saturation vapor pressure we use Tetens' formula

$$q_{vs}=\frac{3.8}{\bar{p}}\exp\left(17.27\frac{\bar{\Pi}\theta-273}{\bar{\Pi}\theta-36}\right). \tag{2.11}$$

The use of mean state pressure is justified by Wilhelmson and Ogura (1972) and by comparison tests with the present model. Eqs. (2.10) and (2.11) are sufficient to uniquely determine θ and q_v in a saturated region in which supersaturation is not permitted. By summing the q_v and q_c equations, we obtain

$$\frac{dq_l}{dt}=D_{q_v}+D_{q_c}+(E_r-A_r-C_r), \tag{2.12}$$

and thus $q_l=q_v+q_c$ is a conservative variable in the absence of rain processes and turbulent mixing.

The procedure used to compute the conversion between water vapor and cloud water has been given by Soong and Ogura (1973). In this procedure the prognostic equations for θ, q_v and q_c are first stepped forward in time, holding $dq_{vs}/dt=0$. Adjustment is then made such that Eqs. (2.10)–(2.12) are satisfied for that time step. Further details of this procedure are included in Section 3b.

Autoconversion (A_r) and accretion (C_r) rates are determined using the Kessler parameterization, where C_r is based on a Marshall–Palmer distribution for q_r. These rates are defined by

$$A_r=k_1(q_c-a), \tag{2.13a}$$

$$C_r=k_2q_cq_r^{0.875}, \tag{2.13b}$$

and we are presently setting $k_1=0.001$ s^{-1}, $a=0.001$ g g^{-1} and $k_2=2.2$ s^{-1}, following Soong and Ogura (1973). Some testing of the sensitivity of results to the value of a is presented in Section 4d. The evaporation of rain is calculated using a rate equation similar to that described by Ogura and Takshashi (1971), i.e.,

$$E_r=\frac{1}{\bar{\rho}}\frac{(1-q_v/q_{vs})C(\bar{\rho}q_r)^{0.525}}{5.4\times10^5+2.55\times10^6/(\bar{p}q_{vs})}, \tag{2.14a}$$

where C is the ventilation factor given by

$$C=1.6+124.9(\bar{\rho}q_r)^{0.2046}. \tag{2.14b}$$

The first term on the right-hand side of (2.9d) represents the vertical flux of rain. The expression for the terminal fall velocity V is similar to that given by Soong and Ogura (1973) but is adjusted for mean density variations as suggested by Kessler (1969) and commented on by Beard (1977):

$$V=3634(\bar{\rho}q_r)^{0.1346}\left(\frac{\bar{\rho}}{\rho_0}\right)^{-\frac{1}{2}}\ [\text{cm s}^{-1}], \tag{2.15}$$

where ρ_0 is the base state density at the ground. In expressions (2.13), (2.14) and (2.15), p is specified in millibars, $\bar{\rho}$ in grams per cubic centimeter, and q_v, q_c and q_r in grams per gram.

c. *Subgrid turbulence parameterization*

Computational constraints in three-dimensional cloud modeling presently require that the numerical grid be rather coarse. In order to include some of the effects of subgrid-scale motion on the resolvable scales we have taken an approach suggested by Deardorff (private communication). In this approach a prognostic equation is solved for subgrid kinetic energy which is used to specify the eddy mixing coefficients. Where appropriate, mixing length theory using these coefficients is then applied to conservative variables.

The subgrid transport and variance terms that require parameterization are derived by performing Reynolds averaging on each of the prognostic variables. The results after averaging are denoted by D_ϕ in (2.4), (2.5) and (2.7) where ϕ is the appropriate prognostic variable. Prognostic equations for the subgrid transports and variances can then also be derived. For example, Deardorff (1973, 1974) and Mellor and Yamada (1974) have used these subgrid prognostic equations for investigation of the near neutrally stable planetary boundary layer capped by a stable layer. This approach, however, triples the number of required prognostic equations and thus is not feasible for three-dimensional cloud modeling at the present time.

Fortunately, significant simplifications can be made to the subgrid equations, while retaining basic features of the subgrid or turbulence statistics (Deardorff, 1975; Mellor and Yamada, 1974: Yamada and Mellor, 1975; Schemm and Lipps, 1976: Sommeria, 1976). In the approach adopted here, the subgrid turbulence equations are simplified and only the prognostic equation for subgrid turbulence energy is retained. As a result, considerable savings in computer time and storage are realized. Such simplifications are, however, used in deep cloud models with some uncertainty for several reasons. One is that measurements of turbulent processes within clouds and storms for verification purposes are minimal. Another is that closure techniques for the subgrid equations are based on the existence of a grid scale within the inertial subrange and with present resolution this requirement is not satisfied. However, we can still evaluate the distribution of subgrid-scale energy based on our understanding of turbulence within growing thermals and with the

aid of some observations of in-cloud variances from Doppler radar. The latter can be used to provide estimates of the magnitude and distribution of energy dissipation on the 0.5–1 km scale (Frisch and Strauch, 1976). Therefore, we feel that a subgrid parameterization based on turbulence energy estimates is justified for a cloud model, especially if it does not require a major increase in computation. In any event, it provides a significant improvement over procedures which define simple nonlinear mixing coefficients based only on shear.

The general approach taken in the following parameterization is to close the subgrid transports using mixing length theory on conservative variables. In unsaturated motion θ and q_v are conserved. In saturated motion q_l is conserved (ignoring rain processes), while (2.10) governs conservation in the thermodynamic processes. Based on these considerations, the expressions for $D_\phi = D_\theta$, D_{q_v}, D_{q_c} and D_{q_r} can be approximated for both unsaturated and saturated motion as

$$D_\phi = -\frac{\partial}{\partial x_j}\overline{(u_j'\phi')} \sim \frac{\partial}{\partial x_j}\left(K_h \frac{\partial \phi}{\partial x_j}\right), \tag{2.16}$$

where K_h is an eddy mixing coefficient to be defined later. Here, primed variables refer to deviations from the grid volume average and overbars denote an average taken throughout the grid volume. At this point we assume that unprimed variables represent grid volume averages and thus their overbars are omitted to avoid confusion with those used for the undisturbed initial state variables.

At first glance, it may not be evident that these expressions provide closure on conservative quantities when the air is saturated. However, as discussed above, the moist processes are governed by Eqs. (2.10)–(2.12) and consequently, the closures denoted in (2.16) imply a closure for (2.10) given by

$$D_\theta + \gamma D_{q_v} = \frac{\partial}{\partial x_j}\left(K_h \frac{\partial \theta_e}{\partial x_j}\right) - K_h q_v \frac{d\gamma}{dz}\cdot\frac{\partial}{\partial z}\left[\ln\left(K_h q_v^2 \frac{d\gamma}{dz}\right)\right] \tag{2.17a}$$

and for (2.12) by

$$D_{q_v} + D_{q_c} = \frac{\partial}{\partial x_j}\left(K_h \frac{\partial q_l}{\partial x_j}\right). \tag{2.17b}$$

Ignoring the z-dependence of γ, Eqs. (2.17) reveal that the condensation adjustment provides closure using the nearly conservative variables θ_e and q_l. [The last term in (2.17a) arises because in the thermodynamic equation (2.10), θ_e is not exactly conserved.] The advantage of this approach is that in solving the θ, q_v and q_c equations, the subgrid mixing terms have the same form regardless of whether or not the air is saturated.

The subgrid momentum terms are given by

$$D_{u_i} = -\frac{\partial}{\partial x_j}\overline{(u_i'u_j')}, \tag{2.18}$$

where

$$\overline{u_i'u_j'} = -K_m\left(\frac{\partial u_i}{\partial x_j} + \frac{\partial u_j}{\partial x_i}\right) + \tfrac{2}{3}\delta_{ij}E. \tag{2.19}$$

Here K_m is the momentum eddy mixing coefficient and E is the subgrid-scale kinetic energy given by

$$E = \tfrac{1}{2}\overline{(u_i')^2}. \tag{2.20}$$

In deriving these expressions, motion on the subgrid scale is assumed incompressible which is a good approximation for motion at scales smaller than the grid interval. The remaining mixing term D_r is set to zero since it has virtually no influence on the solutions.

It now remains to determine E, K_m and K_h. The turbulence energy is represented by a prognostic equation of the form

$$\frac{dE}{dt} = g\overline{w'\left(\frac{\theta'}{\bar\theta} + 0.61q_v' - q_c'\right)} - \overline{u_i'u_j'}\frac{\partial u_i}{\partial x_j} + \frac{\partial}{\partial x_j}\left(K_m\frac{\partial E}{\partial x_j}\right) - (C_\epsilon/l)E^{\frac{3}{2}}, \tag{2.21}$$

where $l = (\Delta x \Delta y \Delta z)^{\frac{1}{3}}$ is the appropriate length scale (Lilly, 1967) and $E \geqslant 0$ is enforced. This equation is similar to that used by Deardorff (1975), Mellor and Yamada (1974), Schemm and Lipps (1976) and others. The terms on the right-hand side of (2.21) represent the effects of buoyancy, shear, diffusion and dissipation. All the subgrid terms have been defined except for the vertical buoyancy flux in saturated motion. This term can be expressed as a function of the nearly conservative variables θ_e and q_l, and then closed using mixing length theory. This is accomplished by relating the saturation mixing ratio and θ through the Clausius–Clapeyron equation which yields

$$\overline{u_i'q_v'} = \frac{\epsilon L q_v}{R_d T\theta}\overline{u_i'\theta'}, \tag{2.22}$$

where $\epsilon = 0.622$. Employing the definition of θ_e, Eq. (2.22) becomes

$$\overline{u_i'\theta'} = \overline{u_i'\theta_e'}\left(1 + \frac{\epsilon L^2 q_v}{c_p R_d T^2}\right)^{-1}. \tag{2.23}$$

Coupling these expressions with (2.3) and closing on

θ_e and q_l yields

$$\overline{w'\left(\frac{\theta'}{\bar{\theta}}+0.61q_v'-q_c'\right)}=-AK_h\frac{\partial\theta_e}{\partial z}+K_h\frac{\partial q_l}{\partial z}, \quad (2.24)$$

$$A=\frac{1}{\bar{\theta}}\left\{\frac{1+\dfrac{1.61\epsilon Lq_v}{R_dT}}{1+\dfrac{\epsilon L^2q_v}{c_pR_dT^2}}\right\}. \quad (2.25)$$

Once E is known, K_m can be determined on dimensional grounds using

$$K_m=C_mE^{\frac{1}{2}}l. \quad (2.26)$$

Following Deardorff (1975), the coefficients are defined by $C_m=C_\epsilon=0.2$. K_h is then related to K_m by a proportionality constant, i.e., $K_h=3K_m$. The factor of 3 was used in Deardorff's (1972) study for unstable and neutral environments in order that the transfer of scalar variance of potential temperature on the grid scale be matched to that calculated on the subgrid scale. Although the subgrid variance has not been retained in the present formulation, we have used the same ratio for K_h/K_m.

The turbulence energy equation (2.21) provides a Richardson number cutoff for turbulence energy. This can be demonstrated by assuming that the buoyancy, shear and dissipation terms are the dominant terms in the equations and by equating these three terms. Considering only vertical gradients of the horizontal velocity, the resulting equation allows for $E>0$ only if $\mathrm{Ri}<K_m/K_h$, where

$$\mathrm{Ri}=\frac{\dfrac{g}{\bar{\theta}}\dfrac{\partial\theta_e}{\partial z}}{\left(\dfrac{\partial u}{\partial z}\right)^2+\left(\dfrac{\partial v}{\partial z}\right)^2}.$$

For $K_m/K_h=\frac{1}{3}$ the cutoff Richardson number is just slightly greater than the accepted value of one quarter.

The dependence of E (and thus K_h) on buoyancy helps alleviate excessive mixing of θ at the top of the mixed layer. Wilhelmson (1974) avoided excessive mixing in an ad hoc way by diffusing only the deviation of θ from its initial value. In the current parameterization K_h is zero just above the mixed layer in the cloud environment because the stability term dominates the shear term in (2.21). Therefore, in the vertical mixing term for the θ equation in Eq. (2.16), $(\partial\theta/\partial z)(\partial K_h/\partial z)$ is negative at the top of the layer and counters the positive $K_h\partial^2\theta/\partial z^2$ term. This has been verified in a boundary layer formulation reported by Deardorff (1975).

d. Boundary conditions

Since the numerical computations take place within a finite domain, appropriate boundary conditions must be specified along all sides of the integration region. The difficulty in choosing these boundary conditions depends, to a large extent, on whether or not flow through the boundary is allowed to take place.

Along the top and bottom of the model domain we require the normal velocity w to vanish. This constraint is correct for the lower boundary and should be reasonable for the upper boundary if that boundary remains a sufficient distance above cloud-top level and if vertical transport of horizontal momentum by gravity waves is not considered important. At these boundaries the appropriate set of well-posed boundary conditions is clearly defined by Oliger and Sundstrom (1976). For inviscid flow the only condition required at $z=0$ and $z=z_T$ is $w=0$. With the eddy mixing (viscous) terms present we need to specify conditions on the normal derivatives of the remaining variables at the boundary to accommodate these terms. Along the boundaries we presently set the normal mixing term equal to zero which is nearly equivalent to assuming that the normal second derivatives vanish at the boundaries. With this approach vertical gradients in the mean state profiles are not distorted due to eddy mixing near the boundaries. This undesirable smoothing does occur with the so called "free slip" condition which requires the normal first derivatives to become zero at the boundaries. It is important to emphasize that boundary conditions required by the presence of small viscous terms should be applied only to these terms. If they are applied to the inviscid portions of the equations, momentum and thermal boundary layers will form which are totally artificial except possibly along the ground.

At the lateral boundaries the situation is more complicated since the locations of the boundaries must be arbitrarily specified. Both mean flow and a variety of wave modes can propagate in and out through these boundaries. For the current cloud model our primary concern is to let disturbances pass out through the lateral boundaries with minimal reflection. Given a set of initial conditions, it is hoped that as a cloud develops within the domain conditions near the boundaries will change in response to that development in about the same way they would if no boundaries were present.

Here again, a set of well-posed boundary conditions has been derived by Oliger and Sundstrom (1976). Their analysis indicates that for inviscid flow all prognostic variables (or certain combinations of them) but one should be specified where the normal velocity is directed into the domain, i.e., for inflow regions. For outflow regions only one boundary condition should be specified. Although these conditions insure stability and continuity of the solution, they do not provide information which enables one to eliminate the reflec-

tion of gravity waves. Conceptually, there are an infinite number of mathematically proper solutions, each corresponding to a different level of wave reflection at the boundary. For this reason we have specified a set of open boundary conditions which makes some attempt to reduce gravity wave reflections at the boundary. The guidelines set down by Oliger and Sundstrom are followed in terms of specifying the correct number of conditions at each boundary. However, it is not clear that these formulations are of the proper form to insure that the system is well-posed.

We consider first an outflow region where one boundary condition is required for inviscid flow. The condition we use is the advection of the normal velocity component out through the boundary at a speed given by the sum of the normal velocity component and an approximated intrinsic phase velocity c_* of the dominant gravity wave modes moving out through the boundary. For example, at an x boundary the expression

$$\frac{\partial u}{\partial t}+(u+c_*)\frac{\partial u}{\partial x}=0 \tag{2.27}$$

replaces the u-momentum equation and the remaining variables are determined from the model equations (using one-sided differences for required normal derivatives). For boundaries normal to the y direction, an expression similar to (2.27) is used which advects v through the y boundaries with the advection velocity $v+c_*$. If the Coriolis force is included, a term is added to the right-hand side of (2.27) for x boundaries given by $f(u-\bar{u})$ and a similar one for y boundaries. This term has little effect on the gravity wave modes but allows rotational effects along the boundaries to be consistent with the interior. The numerical treatment of the boundary equations is discussed in Section 3d.

When inflow occurs eight boundary conditions are needed for the nine prognostic equations. For all variables but the normal velocity and pressure we set the normal derivative equal to zero and thus eliminate the normal advection term in the prognostic equations. The eighth boundary condition replaces the normal momentum equation and has the same form as the outflow condition, which for an x boundary is given by (2.27). However, in this situation u and c_* have opposite signs; c_* is still the outward propagating intrinsic phase velocity but u is directed into the domain. When $|u|>|c_*|$ we set $u+c_*=0$.

The intrinsic gravity wave phase velocity c_* is selected to correspond to the faster propagating internal waves in the system. These waves are long wavelength in the horizontal and have a vertical wavelength of nearly twice the height z_T of the domain. The phase speed resulting from this wave structure is

$$c_*=\frac{Nz_T}{\pi}, \tag{2.28}$$

where N is the average Brunt–Väisälä frequency. For typical values of $z_T=10$ km and $N=0.01$ s^{-1}, the magnitude of c_* is about 30 m s^{-1}. Tests using this and other values of c_* in a two-dimensional model are discussed in Section 4c.

The eddy mixing terms are handled along the lateral boundaries in the same manner as at the top and bottom boundaries by setting the normal mixing term equal to zero. These conditions are in fact of little consequence since the turbulence parameterization is such that the mixing coefficients near the lateral boundaries will usually be zero unless the cloud intersects the boundary.

This lateral boundary formulation is similar in many respects to that proposed by Klemp and Lilly (1978) in a model for simulating hydrostatic mountain waves. Analysis of wave reflection at a boundary was also presented in this paper based on the similarities between the hydrostatic equations and the shallow water equations. Although wave propagation in the nonhydrostatic equations is considerably more complicated, portions of the boundary behavior can be analyzed to provide some justification for our choice of boundary conditions. For this purpose, we shall illustrate the reflection produced at an outflow boundary in the two-dimensional linear equations when a periodic gravity wave of the form

$$\begin{aligned} u_1&=\hat{u}_1\exp[i(k_1x+lz-\omega_1t)],\\ \omega_1&=k_1\bar{u}+\frac{k_1N}{(k_1^2+l^2)^{\frac{1}{2}}} \end{aligned} \tag{2.29}$$

impinges upon the boundary. This expression for ω_1 is obtained from the dispersion relation for the downstream propagating gravity wave mode with $\bar{u}>0$ being the mean wind. If a boundary condition is specified which is not compatible with this mode, reflection can in general take place into an upstream propagating gravity wave mode which has the form

$$\begin{aligned} u_2&=\hat{u}_2\exp[i(k_2x+lz-\omega_2t)],\\ \omega_2&=k_2\bar{u}-\frac{k_2N}{(k_2^2+l^2)^{\frac{1}{2}}}. \end{aligned} \tag{2.30}$$

A reflection coefficient can then be defined as $r=|\hat{u}_2/\hat{u}_1|$. The intrinsic phase speed of the two gravity wave modes are identified as

$$c_1=\frac{N}{(k_1^2+l^2)^{\frac{1}{2}}},\quad c_2=\frac{N}{(k_2^2+l^2)^{\frac{1}{2}}}. \tag{2.31}$$

Along the outflow boundary the frequency of the incident and reflected modes must match if the sum of the two modes is to satisfy the specified boundary condition. Setting $\omega_1=\omega_2$ yields

$$k_2=k_1\frac{\bar{u}+c_1}{\bar{u}-c_2} \tag{2.32}$$

and consequently reflection from the outflow boundary occurs into a higher horizontal wavenumber than that of the incident mode. The reflectivity caused by the boundary condition can then be estimated by substituting $u=u_1+u_2$ into the condition and solving for r. This procedure is essentially the same as that used by Nitta (1964) and Matsuno (1966) in analyzing outflow boundary conditions. Inserting (2.29) and (2.30) into (2.27) yields

$$r=\left|\frac{\bar{u}-c_2}{\bar{u}+c_1}\cdot\frac{c_1-c_*}{c_2+c_*}\right|. \tag{2.33}$$

Notice that as c_* approaches c_1 the reflection is eliminated, but even if c_* is poorly chosen r will be less than unity. This expression also indicates that less reflection is caused by overestimating c_* than by underestimating it by the same amount. For this reason c_* is chosen to correspond to the faster propagating modes as mentioned above.

If $c_2<\bar{u}$, both gravity wave modes will be swept downstream. For the hydrostatic equations specifying an outflow boundary condition for this situation would lead to an ill-posed problem (Oliger and Sunderstrom, 1976). However, with the compressible, nonhydrostatic equations the system remains well posed. Reflection still occurs into mode u_2, but now k_2 becomes complex. Analysis indicates that the reflected mode can then propagate upstream and that it is progressively damped out as it moves away from the boundary. This result can be inferred from (2.31) and (2.32) which have real solutions for k_2 only if $c_2>\bar{u}$.

At inflow a similar analysis can be conducted. In this case u_2 would be the incident mode and u_1 the reflected one. Since (2.32) must again be satisfied, reflections from the inflow boundary will take place into longer horizontal wavelengths.

This type of analysis greatly oversimplifies the results which would be expected in the actual model. Further, we must realize that as the numerical resolution of propagating modes decreases, reflection at the boundary can be expected to increase. However, from a practical point of view, these boundary conditions appear to be stable in the absence of any computational damping and to reduce wave reflection to tolerable levels.

In addition to allowing disturbances to pass out of the domain, time-dependent conditions (based on a larger scale flow) can be imposed at the lateral boundaries. This is accomplished by including terms representing the time rate of change of the boundary forcing in the prognostic equations at the boundary. For example, at an x boundary the prognostic equation for u is changed from (2.27) to

$$\frac{\partial u}{\partial t}+(u+c_*)\frac{\partial u}{\partial x}=\left(\frac{\partial u}{\partial t}\right)_B \tag{2.34}$$

and other boundary equations are similarly altered. In the linear system modes forced at the boundary do not interact with disturbances propagating out from the interior and thus the boundary reflection is not affected by this forcing.

3. Representation of the finite-difference equations

In constructing the numerical framework for a three-dimensional cloud model we must balance the relative advantages of procedures which reduce the number of computations against alternatives which may reduce the amount of data stored at each grid point. In this regard the choice of a grid structure and the selection of a time-differencing scheme are particularly significant. For our grid system we have chosen the standard spatially staggered mesh (e.g., Wilhelmson, 1974) in which all thermodynamic and moisture variables are defined at a common point and the velocity components u_i are displaced by one-half grid interval $\frac{1}{2}\Delta x_i$. With this staggering, the resolution of the pressure terms in (2.4) and of the divergence term in (2.6) is greater than that achieved in the unstaggered case. Since the time step limitations for linear stability in our simulations are primarily determined by the advection and mixing terms which do not involve mesh staggering, the staggered mesh does not require a reduced time step.

The time-differencing scheme for portions of the calculations which do not involve sound waves is second-order leapfrog. The advantages of this scheme are that it requires only a single step computation for each time step and that no computational damping is present. The main disadvantage is that two time levels must be stored for each prognostic variable. However, other second-order time-differencing schemes commonly considered require two step procedures (c.f. Crowley, 1968; Matusno, 1966) and have varying degrees of computational damping. In comparison with leapfrog, such techniques require approximately twice as many computations with approximately the same amount of data transfer per time step with careful programming. Although the actual large core space requirements for leapfrog are nearly double those of other methods, we feel this drawback is outweighed by the computational efficiency and the lack of computational damping in the leapfrog scheme. Using leapfrog differencing, time splitting has not caused any significant problems.

For convenience in describing the finite difference representations, we follow Lilly (1965) in defining the finite-difference operators

$$\begin{aligned}\delta_{n\xi}\phi(\xi)&=(1/n\Delta\xi)[\phi(\xi+n\Delta\xi/2)-\phi(\xi-n\Delta\xi/2)],\\ \overline{\phi(\xi)}^{n\xi}&=\tfrac{1}{2}[\phi(\xi+n\Delta\xi/2)+\phi(\xi-n\Delta\xi/2)].\end{aligned} \tag{3.1}$$

Here ϕ denotes the dependent variable, ξ the independent variable, and $n\Delta\xi$ is interval over which the operation takes place.

a. Numerical framework for the dynamic equations

In solving the compressible equations of motion, the presence of sound waves severely limits the magnitude of the time step in explicit differencing schemes. For this reason, we achieve numerical efficiency in the model by treating the sound wave modes separately on a small time step as proposed by Klemp (1978). With this procedure all other processes can then be computed using a larger time step which is appropriate for the time scales of physical interest.

To use this technique, we begin by identifying the terms responsible for sound wave generation in the model equations. Collecting these terms on the left-hand side, Eqs. (2.4) and (2.7) become

$$\left.\begin{aligned} &\frac{\partial u_i}{\partial t}+c_p\bar{\theta}_v\frac{\partial \pi}{\partial x_i}=f_{u_i}\\ &\frac{\partial \pi}{\partial t}+\frac{\bar{c}^2}{c_p\bar{\rho}\bar{\theta}_v^2}\frac{\partial}{\partial x_j}(\bar{\rho}\bar{\theta}_v u_j)=f_\pi \end{aligned}\right\}. \tag{3.2}$$

Here f_{u_i} and f_π represent all the remaining terms in (2.4) and (2.7) and as discussed in the previous section, ignoring f_π causes little alteration to the results. The remaining equations have no fundamental influence on sound waves and can thus be solved using time steps which would be appropriate if sound waves were not present.

The splitting procedures for solving (3.2) will be presented by Klemp (1978) and are summarized here. Let Δt correspond to the relatively large time step which is appropriate for the processes of physical interest. We seek to step Eqs. (3.2) from time level $t-\Delta t$ forward to $t+\Delta t$, evaluating the right-hand sides f_{u_i} at the middle level t. To maintain stability for the sound wave modes this overall step is accomplished by dividing it into a series of smaller steps, each with a time step $\Delta\tau$. Since our vertical grid interval is typically smaller than the horizontal mesh size, improved efficiency is achieved by having each of these smaller steps be semi-implicit in the vertical, with a finite-difference representation given by

$$\delta_\tau u+c_p\bar{\theta}_v\delta_x\pi^\tau=f_u^t,\quad \delta_\tau v+c_p\bar{\theta}_v\delta_y\pi^\tau=f_v^t, \tag{3.3}$$

$$\left.\begin{aligned} &\delta_\tau\tilde{w}+c_p\bar{\rho}\bar{\theta}_v^2\overline{\delta_z\pi}^{\tau}=\bar{\rho}\bar{\theta}_v f_w^t\\ &\delta_\tau\pi+\frac{\bar{c}^2}{c_p\bar{\theta}_v}(\delta_x u+\delta_y v)^{\tau+\Delta\tau}+\frac{\bar{c}^2}{c_p\bar{\rho}\bar{\theta}_v^2}\overline{\delta_z\tilde{w}}^{\tau}=0 \end{aligned}\right\}. \tag{3.4}$$

The variable τ indicates the time level for these small time steps and increases from 0 to $2\Delta t$ during the $n=2\Delta t/\Delta\tau$ steps associated with each large step and the time differences in (3.3) and (3.4) are between τ and $\tau+\Delta\tau$. For convenience and to save a few computations in the integrations we have defined $\tilde{w}=\bar{\rho}\bar{\theta}_v w$ (only for the small time step calculations). These equations are linear in form with coefficients which vary only in z. For each small time step Eqs. (3.3) are stepped forward and then Eqs. (3.4) are solved by inverting a tri-diagonal matrix in the vertical to obtain π. For stability $\Delta\tau$ must satisfy the restriction

$$\Delta\tau<\frac{1}{c}\left\{\frac{1}{\Delta x^2}+\frac{1}{\Delta y^2}\right\}^{-\frac{1}{2}}, \tag{3.5}$$

while Δt is limited by the linear stability criteria for the non-sound wave processes. A more detailed description of the stability of this numerical procedure will be presented separately (Klemp, 1978).

As an example, for $\Delta x=\Delta y=1$ km, $\Delta\tau$ can be as large as 2 s regardless of the magnitude of Δz. Using $\Delta t=10$ s for the large time step calculations then would require $n=10$ small time steps to integrate (3.3) and (3.4) forward from $t-\Delta t$ to $t+\Delta t$. Since the number of computations for each small time step is only a small fraction of that required for the large time step, the operational efficiency is not drastically impaired by the existence of sound waves.

Turning to the numerical procedures for the large time step processes, we recognize that the advection terms play an important role in translating disturbances throughout the domain. Insufficient numerical resolution of these terms leads to phase errors which can significantly distort the smaller scale features of a simulation. For this reason, we seek to reduce these errors by approximating the horizontal advection terms with fourth-order finite differences. These differences, in fact, require very few additional computations. Second-order accuracy is maintained for the vertical advection terms since the typically smaller vertical grid interval compensates for the lower order finite-difference approximation. Although the horizontal fourth-order differences do not insure numerical conservation of certain second-order quantities [as is possible with second-order differencing (e.g., Lilly, 1965)] we feel they are desirable because of the increase in numerical accuracy which they provide.

The right-hand sides of the momentum equations, f_{u_i}, are computed on the large time intervals and held fixed during the n small time steps required to step u_i and π forward from $t-\Delta t$ to $t+\Delta t$. Including fourth-order representation of the horizontal advection terms leads to the following difference expressions:

$$\left.\begin{aligned} f_u=&-\tfrac{1}{3}u(4\delta_{2x}u-\delta_{4x}u)-\tfrac{1}{3}\overline{\bar{v}^x}^y(4\delta_{2y}u-\delta_{4y}u)\\ &-\overline{\bar{w}^x\delta_z u}^z+f\overline{\bar{v}^x}^y+D_u\\ f_v=&-\tfrac{1}{3}\overline{\bar{u}^y}^x(4\delta_{2x}v-\delta_{4x}v)-\tfrac{1}{3}v(4\delta_{2y}v-\delta_{4y}v)\\ &-\overline{\bar{w}^y\delta_z v}^z-f\overline{\bar{u}^y}^x+D_v\\ f_w=&-\tfrac{1}{3}\overline{\bar{u}^x}^z(4\delta_{2x}w-\delta_{4x}w)\\ &-\tfrac{1}{3}\overline{\bar{v}^y}^z(4\delta_{2y}w-\delta_{4y}w)-w\delta_{2z}w\\ &+g\left\{\frac{\bar{\theta}^z}{\bar{\theta}}-1+0.61(\overline{q_v}^z-\bar{q}_v)-\overline{q_c}^z-\overline{q_r}^z\right\}+D_w \end{aligned}\right\}. \tag{3.6}$$

The remaining equations for θ, q_v, q_c and q_r from (2.8) all have a similar finite-difference representation given by

$$\delta_{2t}\phi = -\tfrac{1}{3}\bar{u}^x(4\delta_{2x}\phi - \delta_{4x}\phi) - \tfrac{1}{3}\bar{v}^y(4\delta_{2y}\phi - \delta_{4y}\phi) - \overline{w\delta_z\phi}^z + M_\phi + D_\phi, \quad (3.7)$$

where ϕ denotes any one of these four prognostic variables. Numerical treatment of the microphysical terms M_ϕ and the subgrid mixing terms D_ϕ is discussed in the next two subsections.

b. Numerical representation of the microphysics

Under saturated conditions, the condensation-evaporation processes are numerically evaluated by solving the thermodynamic and moisture equations using a two-step procedure proposed by Soong and Ogura (1973). In the first step the θ, q_v and q_c equations are stepped forward to time level $t+\Delta t$ with the dq_{vs}/dt terms set equal to zero. Values computed from this step are denoted with an asterisk. Since (2.10) is valid independent of the amount of condensation or evaporation taking place, in the adjustment step we require

$$\theta^{t+\Delta t} + \gamma q_v^{t+\Delta t} = \theta^* + \gamma q_v^*. \quad (3.8)$$

In addition, Tetens' formula (2.11) is linearized about $\theta=\theta^*$ to yield

$$q_v^{t+\Delta t} = q_{vs}^{t+\Delta t} \approx q_{vs}^*\left[1 + \frac{4093a\bar{\Pi}}{(\bar{\Pi}\theta^* - 36)^2}(\theta^{t+\Delta t} - \theta^*)\right], \quad (3.9)$$

where q_{vs}^* is the solution of (2.11) for $\theta=\theta^*$. Eqs. (3.8) and (3.9) can then readily be solved for $\theta^{t+\Delta t}$ and $q_v^{t+\Delta t}$. Having determined $q_v^{t+\Delta t}$, the conservation equation (2.12) provides the following relation for $q_c^{t+\Delta t}$:

$$q_v^{t+\Delta t} + q_c^{t+\Delta t} = q_v^* + q_c^*, \quad (3.10)$$

together with the requirement that $q_c^{t+\Delta t} \geqslant 0$. Although the individual equations for θ, q_v and q_c were solved in the first step, the adjustment makes the entire procedure equivalent to having solved the nearly conservative equations (2.10) and (2.12). For this reason, in a saturated environment the subgrid closures given by (2.16) effectively close the system on the conservative variables described by (2.17).

The derivative of the rain flux is computed at all but the lowest level using a centered approximation, i.e.,

$$\frac{\partial}{\partial z}(\bar{\rho}Vq_r) = \delta_{2z}(\bar{\rho}Vq_r). \quad (3.11)$$

At the lowest level an upstream approximation is used and the fluxes lagged at $t-\Delta t$ to maintain linear stability. Presently any negative rainwater arising because of the centered difference in (3.11) is adjusted back to zero.

c. Numerical representation of the subgrid-scale equations

To increase coding efficiency the subgrid-scale kinetic energy equation (2.21) is actually written in terms of K_m (using (2.26) and assuming that l is constant). This equation then has a finite difference form given by

$$\delta_{2t}K_m = -\tfrac{1}{3}\bar{u}^x(4\delta_{2x}K_m - \delta_{4x}K_m) - \tfrac{1}{3}\bar{v}^y(4\delta_{2y}K_m - \delta_{4y}K_m) - \overline{w\delta_zK_m}^z + \frac{C_m^2l^2}{2K_m}(B+S) + \tfrac{1}{2}(\delta_{xx}K_m^2 + \delta_{yy}K_m^2 + \delta_{zz}K_m^2) - \frac{C_\epsilon K_m^3}{2C_ml^2}. \quad (3.12)$$

The last two terms in (3.12) are evaluated at $t-\Delta t$ in order to maintain numerical stability. The B term is the buoyancy term and its evaluation depends on whether or not the air is saturated ($q_c>0$). When $q_c=0$,

$$B = -g\frac{K_h}{\theta}\delta_{2z}\theta \quad (3.13a)$$

and when $q_c>0$

$$B = -gAK_h\delta_{2z}\theta_e + gK_h\delta_{2z}q_l, \quad (3.13b)$$

where A represents the term defined in (2.25).

In (3.12), S represents the shear term and is approximated by

$$S = -\overline{u_i'u_j'}\frac{\partial u_i}{\partial x_j} = K_m\left\{2[(\delta_xu)^2 + (\delta_yv)^2 + (\delta_zw)^2] + (\overline{\delta_xv+\delta_yw}^{yz})^2 + (\overline{\delta_xw+\delta_zu}^{xz})^2 + (\overline{\delta_yw+\delta_zv}^{yz})^2\right\}. \quad (3.14)$$

The subgrid terms in the momentum equations are represented using (2.19) as

$$D_u = 2\delta_x(K_m\delta_xu) + \delta_y[\bar{K}_m^{xy}(\delta_yu+\delta_xv)] + \delta_z[\bar{K}_m^{xz}(\delta_zu+\delta_xw)] - \frac{2}{3C_m^2l^2}\delta_xK_m^2, \quad (3.15a)$$

$$D_v = \delta_x[\bar{K}_m^{xy}(\delta_xv+\delta_yu)] + 2\delta_y(K_m\delta_yv) + \delta_z[\bar{K}_m^{yz}(\delta_zv+\delta_yw)] - \frac{2}{3C_m^2l^2}\delta_yK_m^2, \quad (3.15b)$$

$$D_w = \delta_x[\bar{K}_m^{xz}(\delta_xw+\delta_zu)] + \delta_y[\bar{K}_m^{yz}(\delta_yw+\delta_zv)] + 2\delta_z(K_m\delta_zw) - \frac{2}{3C_m^2l^2}\delta_zK_m^2. \quad (3.15c)$$

Finally, the subgrid calculations for $\phi=\theta$, q_v and q_c are represented represented by

$$D_\phi = \delta_x(\bar{K}_h^x\delta_x\phi) + \delta_y(\bar{K}_h^y\delta_y\phi) + \delta_z(\bar{K}_h^z\delta_z\phi). \quad (3.16)$$

The expressions (3.15) and (3.16) for the mixing terms are computed at time $t-\Delta t$ to maintain stability.

d. Numerical treatment of boundary conditions

Using a spatially staggered grid network, the finite-difference equations can be solved near the boundary with less difficulty than in an unstaggered framework. With the w grid points placed at the top and bottom boundaries, all other variables are located within the domain. Thus, by specifying $w=0$ at $z=0$ and $z=z_T$, no alteration is required for the remaining equations near the boundary except to eliminate the normal component of the damping terms.

At lateral boundaries only the grid points corresponding to the normal component of velocity are located along the boundary. However, at an outflow boundary, normal derivatives must be calculated for each of the prognostic variables located at or adjacent to the boundary. These are computed with a first-order, accurate, one-sided difference lagged at time $t-\Delta t$ to provide stability. At inflow only the normal velocity gradient is required and it is computed in a similar manner. One grid point in from a lateral boundary the normal horizontal advection terms are approximated using a second-order difference instead of the fourth-order one used elsewhere.

e. Numerical smoothing

As mentioned earlier, time splitting due to the leapfrog scheme is not a significant problem in the model. However, to remove any tendencies which might tend to decouple the odd and even time steps, a time smoother proposed by Robert (1966) is incorporated in the model. This smoother is described by the algorithm

$$\left.\begin{aligned}\phi^{*t+\Delta t}&=\phi^{t-\Delta t}+2\Delta t F^{*t}\\ \phi^{t}&=\phi^{*t}+\alpha(\phi^{*t+\Delta t}-2\phi^{*t}+\phi^{t-\Delta t})\end{aligned}\right\}. \quad (2.13)$$

The first equation denotes the leapfrog step for $\partial\phi/\partial t=F$ with the asterisk representing terms which have not yet been smoothed by the second step. The damping characteristics of this technique have been analyzed by Asselin (1972) and found to produce strong damping on the computational mode with little impact on the physical modes. At present, α is set at 0.1. Although this filter is applied every time step it requires few extra computations, no additional storage, and has a smoother impact on the solution than filters which are applied only once in a rather large number of time steps.

In applying this filter several minor points deserve mention. The variable $\phi^{*t+\Delta t}$ should represent the final value calculated for this variable at $t+\Delta t$ with the exception of time smoothing. Because our condensation procedure adjusts θ, q_v and q_c after they have been stepped forward in time, smoothing the middle time level for these variables should follow this adjustment. Also, if the filter is applied to the velocity variables it must also be used on pressure to maintain stability.

The subgrid mixing terms provide smoothing related to turbulent processes in the region where $K_m>0$. However, because the buoyancy term prohibits the growth of turbulence energy in most stable regions outside the cloud, $K_m=0$ over large portions of the domain. A small amount of background damping is probably desirable throughout the domain to discourage the growth of nonlinear instabilities and to filter out very short wavelength modes which are likely of spurious origin. For these reasons we have included small fourth-order horizontal damping terms in each of the prognostic equations except pressure which has the finite-difference form

$$-K_D\{\delta_{xxxx}\phi+\delta_{yyyy}\phi\}. \quad (3.13)$$

K_D is then adjusted to be small enough so that the resolvable scales of the simulations are not affected. For the model runs presented here, we found $K_D\Delta t/\Delta x^4=0.0025$ to be a satisfactory value. By using fourth-order derivatives instead of second-order, the damping is much more specific to the removal of the high wavenumber modes.

f. The model code

Since the model code requires a large amount of computing time and frequent transfers of data between main memory and auxiliary storage, careful planning is required in order to efficiently use the available computer system. For example, the current model, although quite small, requires about 30 min of computer time for each hour of simulation time on NCAR's CDC 7600. Further, it requires two data transfers of all three-dimensional fields between main memory and auxiliary storage every large time step and one transfer of a portion of the variables each small time step. Since the model is continually undergoing changes, emphasis is also placed on maintaining flexibility within the code to allow ease in making modifications. This includes changes in the number of grid points, in the physical processes, in the numerical approximations and in the boundary conditions. In order to use the computer system efficiently such changes should require minimal adjustments to the part of the code that handles data transfers.

To accomplish this we have chosen to help in the development and testing of a collection of routines known as FLOW. These routines were designed by Dan Anderson (personal communication) at NCAR. A considerable effort has been required in the development stage; however, the flexibility it has allowed in code modification has already been of value.

The FLOW routines allow the user to access large out-of-core data bases in an efficient manner with

very little effort. Considerable flexibility exists in that changing such features as the number of variables, the grid structure, or the stencil required for calculations at each grid point can be accomplished simply by altering several constants at the beginning of the program. In addition these routines expand the variables into one-dimensional arrays with standard subscripts throughout the model code which improves the computational efficiency.

The FLOW routines are used to transfer data by lines. In this regard, we transfer data by vertical columns since the implicit part of the small time step discussed in Section 3a requires all the data in one column at the same time. Neighboring lines required in a line computation are available as specified by the user. For example, a fourth-order advection scheme requires five lines in both the x and y directions in our code. These data are simply requested in the standard FORTRAN loop structure. Linked lists are used to keep track of the data at a reasonable cost. They require a minimal amount of storage in handling the potential problem of writing results over data that are still required. Output routines are also readily available for displaying data.

4. Model results for idealized cases

Before attempting simulations of observed convective storms, it is instructive to evaluate the model results for simplified atmospheric conditions which can be more easily analyzed. Within such a framework the important physical and numerical formulations in the model can be isolated to a certain extent and tested for accuracy and sensitivity. Although the physical results will be greatly oversimplified, this approach allows one to gain some confidence in the overall model performance before turning to more complex situations.

a. Model initialization and integration

For all of the three-dimensional simulations to be described, the integration domain is 24 km in both horizontal directions and 10 km in the vertical, with horizontal grid intervals of $\Delta x=\Delta y=1000$ m and $\Delta z=500$ m. Although this resolution is admittedly rather coarse, it is operationally convenient since the entire model can be contained within the large core memory of the CDC 7600 and computer time requirements for individual runs are not excessive.

To initiate convection, a low-level temperature perturbation is inserted in the central portion of the domain which has the form

$$\Delta\theta=\Delta\theta_0\cos^2\tfrac{1}{2}\pi\beta \quad \text{for } \beta<1, \tag{4.1}$$

where

$$\beta=\left[\left(\frac{x-x_c}{x_r}\right)^2+\left(\frac{y-y_c}{y_r}\right)^2+\left(\frac{z-z_c}{z_r}\right)^2\right]^{\frac{1}{2}}. \tag{4.2}$$

Here, the subscript c refers to the location of the center of the perturbation, while r denotes its radial dimension in each direction. Defining the origin of the coordinate system to be at the ground and in the center of the domain, we specify $x_c=y_c=0$, $z_c=1500$ m, $x_r=y_r=10.8$ km, $z_r=2000$ m and $\Delta\theta_0=1.5$°C. Although this perturbation is rather large, it is advantageous for testing purposes since it promotes the development of strong convection in a relatively short period of time.

For the initial moisture field, one can either specify the mixing ratio directly or define the water content in terms of a relative humidity profile $H(z)$. Choosing the latter approach requires several iterations of the hydrostatic equation

$$\delta_z\bar{\Pi}=-\frac{g}{c_p\bar{\theta}_v^{-z}} \tag{4.3}$$

and

$$q_v=H(z)q_{vs}(\bar{\Pi},\theta) \tag{4.4}$$

since $\bar{\theta}_v$ is related to $\bar{q}_v$ by (2.3). Within the initial potential temperature perturbation described by (4.1) and (4.2), q_v will be increased in the region of the perturbation when computed from (4.4).

With the Coriolis terms present, we adjust the initial undisturbed potential temperature and pressure fields to provide a geostrophic balance with the initial wind field while maintaining the hydrostatic balance. Thus, by combining the expressions

$$c_p\bar{\theta}_v\pi_x=f\bar{v}, \quad c_p\bar{\theta}_v\pi_y=-f\bar{u}, \quad c_p\bar{\theta}_v\pi_z=g\theta_g/\bar{\theta},$$

we obtain the geostrophic adjustment θ_g given by

$$\theta_g=\frac{f}{g}\bar{\theta}_v\left[\left(\bar{v}_z-\frac{(\bar{\theta}_v)_z}{\bar{\theta}_v}\bar{v}\right)x-\left(\bar{u}_z-\frac{(\bar{\theta}_v)_z}{\theta_v}\bar{u}\right)y\right].$$

Including the low-level perturbation $\Delta\theta$ the initial potential temperature field becomes $\theta=\bar{\theta}+\theta_g+\Delta\theta$, while the hydrostatically balanced perturbation pressure field is obtained from the vertical integration of

$$\delta_z\pi=\frac{g}{c_p\bar{\theta}_v^2}\left[\frac{\overline{\theta-\bar{\theta}}^{z}}{\bar{\theta}}+0.61(q_v-\bar{q}_v)\right], \tag{4.5}$$

with the boundary condition

$$\pi_T=\frac{f}{c_p\bar{\theta}_{vT}}(\bar{v}_Tx-\bar{u}_Ty).$$

along the top of the domain. An alternative procedure is to balance the perturbation pressure field through solution of an elliptic equation as used for the anelastic system. This approach was also tested in the model and was found to produce almost no alteration of the results.

The initial temperature and moisture profiles chosen for these idealized cases are depicted in Fig. 1 by the

solid lines. The initial temperature and moisture perturbations at the center of the domain are also included in the figure, indicated by the corresponding dashed lines. For this sounding the surface pressure is 965 mb. For these simulations the Coriolis force is not included since it is unlikely to have any significant influence during the relatively short integration times presented here. This effect will be included in future simulations which will be of longer duration.

Integrating the model forward in time, the splitting procedure described in Section 2a is employed to improve the computational efficiency in solving the compressible equations. For the large time step we set $\Delta t = 10$ s while for the small time step we use $\Delta \tau = 2$ s. As described in Section 3a the large time step is now 10 times larger than would be required if the equations were integrated using conventional explicit techniques. For the domain size described above, the required CDC 7600 computer time is about half the physical simulation time for a given run. Relative to the total run time, about 30% of the computer time is spent on the small time step which is roughly comparable to the proportion required for solving the Poisson equation in reported anelastic models.

From a conceptual viewpoint, the simplest case to consider is the one in which there is initially no shear present in the atmosphere. Since the initial temperature perturbation (4.1) is axisymmetric in each horizontal plane about the point $x_c = y_c = 0$, the resulting cloud development will also be axisymmetric. Fig. 2 illustrates this solution at $t = 24$ min which is when the updraft has achieved its maximum intensity. Here the u, w, q_c and q_r fields are displayed using vertical cross sections taken along the $y = 0$ axis. Owing to the axisymmetry, this plane reveals the solution throughout the three-dimensional domain. Although the maximum updraft velocity has reached 24 m s^{-1}, the compensating downdrafts are quite weak. Most of the subsidence occurs very gradually over an area which is large compared to that of the updraft. In two-dimensional slab simulations, subsidence tends to be much stronger because of the reduction in area of the surrounding environment. As the integration continues the negative buoyancy associated with water loading subsequently causes the cell to decay fairly rapidly.

In Fig. 1, the heavy solid line represents the maximum potential temperature attained at each level along the centerline of the cloud. This curve appears to be produced by the warmest parcel of air rising through the center of the cloud, and very nearly follows the path of a moist adiabat through the lower and middle levels of the cloud. This adiabat corresponds closely to that which results in lifting a parcel dry adiabatically from the ground to its condensation level at about 870 mb. The moist adiabatic lapse rate within the cloud indicates that the central portion of the updraft is essentially unmixed for this case of an unsheared environment. In observational cases studied in

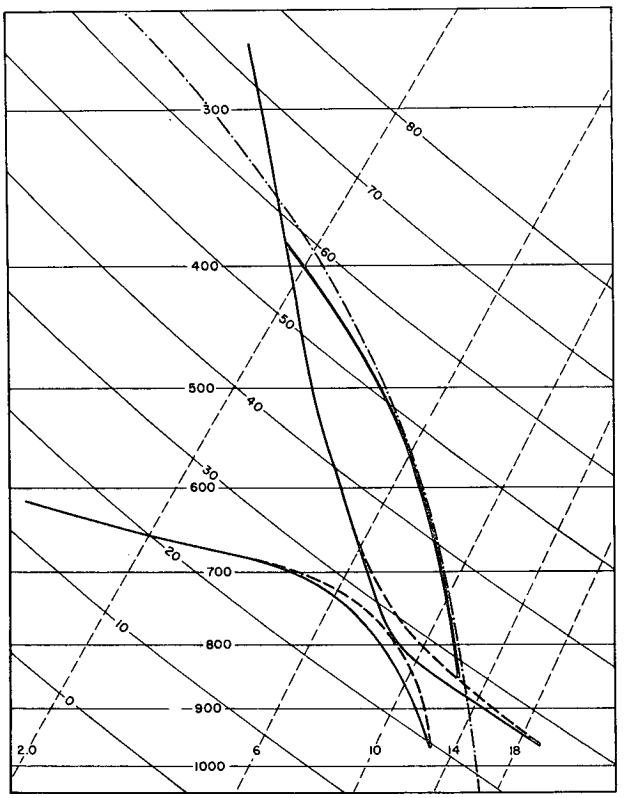

FIG. 1. Skew T diagram depicting initial temperature and moisture profiles. Coordinate lines denote pressure (mb), potential temperature (°C) and mixing ratio (g kg^{-1}). The dot-dashed line represents the 21°C moist adiabat.

Oklahoma, Davies-Jones (1974) measured temperature profiles within clouds which closely followed moist adiabatic lapse rates to mid-levels. Fig. 1 indicates that the cloud develops up to 6°C of buoyancy which provides sufficient forcing to produce the strong convection apparent in Fig. 2.

The presence of vertical wind shear in the atmosphere provides the potential for more interesting cloud development. Under the proper conditions a cloud can sustain itself by forcing rain to fall outside the updraft and by orienting adjacent downdrafts such that they do not cut off the low-level moisture supply. Even small amounts of shear begin to significantly alter cloud structure. This is illustrated by reconsidering the cloud development in the atmosphere described by Fig. 1 when 10 m s^{-1} of shear is present across the lower third of the domain. The initial u field has a vertical profile as depicted in Fig. 3. With the symmetrical initial perturbation (4.1), the ensuing solution is symmetrical about the $y = 0$ plane.

The u, w, q_c and q_r fields in the $y = 0$ plane are shown in Fig. 4 at 24 min. At this time the updraft is somewhat weaker than in the no shear case (Fig. 2) caused in part by the increased subgrid mixing along the upshear (left) side of the cloud. This increased mixing is due to the strong horizontal gradients produced by the inter-

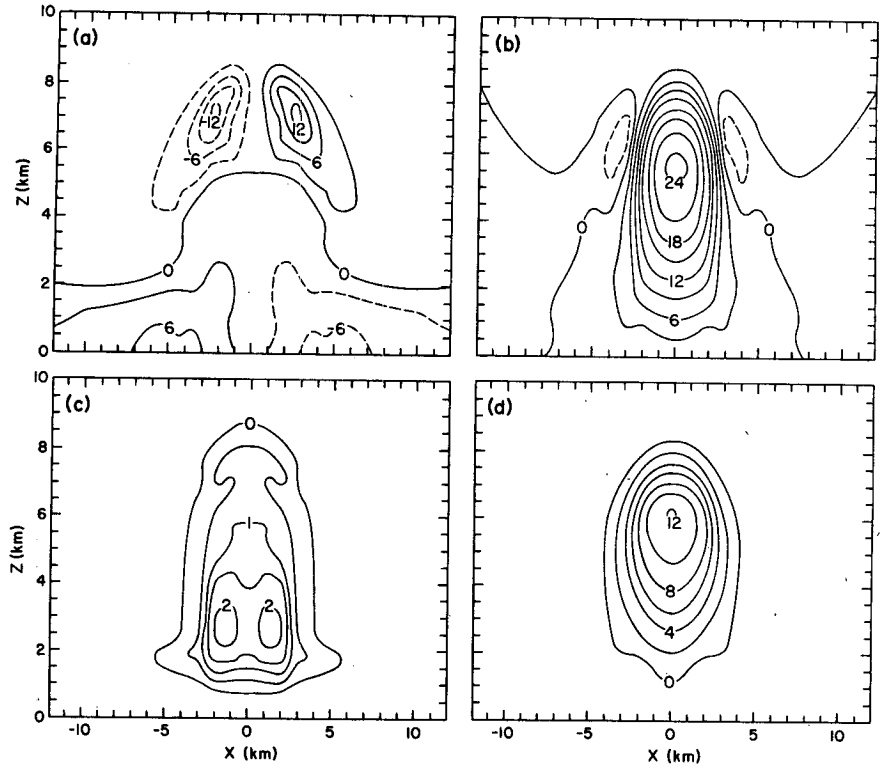

FIG. 2. x-z cross sections at $y=0$ for no-shear simulation at 24 min: (a) u field (m s^{-1}), (b) w field (m s^{-1}), (c) q_c field (g kg^{-1}), (d) q_r field (g kg^{-1}).

action of mid-level environmental air moving toward the right with updraft air moving toward the left.

At 36 min the cloud structure has responded to the development of a downdraft as shown in Figs. 5 and 6. Fig. 5 is similar to Fig. 4 except that $\theta-\bar{\theta}$ is shown in place of q_c. The strong variations in $\theta-\bar{\theta}$ near the top of the domain are caused by gravity waves forming in the stable air above the cloud. Fig. 6 displays horizontal planes of w, $\theta-\bar{\theta}$, q_c and q_r at $z=2.75$ km (2.5 km for w). The downdraft has formed due to water loading along the right side of the cloud and has split the initial updraft (Figs. 5b and 6a). The vertical velocity and cloud water fields have local maxima on either side of the line of symmetry (Figs. 6a and 6c). However, only one maximum exists in the temperature and rainwater fields (Figs. 6b and 6d). The significance of the structure at 36 min is that it appears to have the potential for being self-sustaining. Moisture is being supplied to the updrafts primarily through low-level inflow through the boundaries at $y=\pm 12$ km. At this time the maximum low-level inflow through these boundaries has increased to 5 m s^{-1}. The original primary inflow from the right ($x=12$ km) has been blocked by the downdraft (Figs. 5a and 5b). The rain is falling out in between the updrafts (Fig. 6d) and thus does not block the low level inflow in the y direction. The associated downdraft may instead encourage updraft development as it spreads out near the ground and helps lift the inflowing air. This splitting process is currently being investigated in detail through longer simulations and by varying the low-level environmental shear.

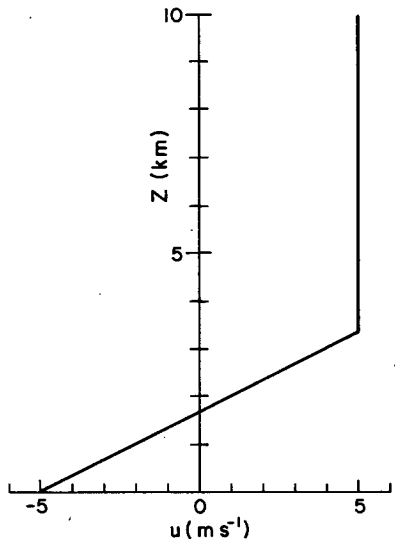

FIG. 3. Initial profile for u component of horizontal velocity for one-directional shear simulation.

b. Evaluation of the turbulence parameterization

In the simulations described above the eddy mixing coefficient was obtained from the turbulence energy

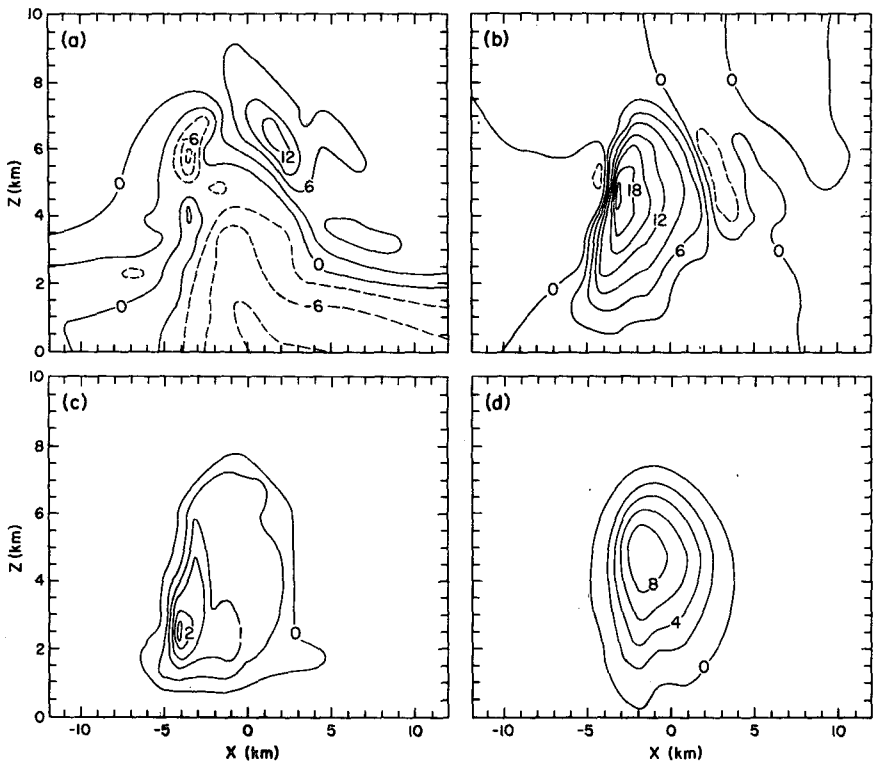

FIG. 4. x-z cross sections at $y=0$ for one-directional shear simulation at 24 min: (a) u field (m s^{-1}), (b) w field (m s^{-1}), (c) q_c field (g kg^{-1}), (d) q_r field (g kg^{-1}).

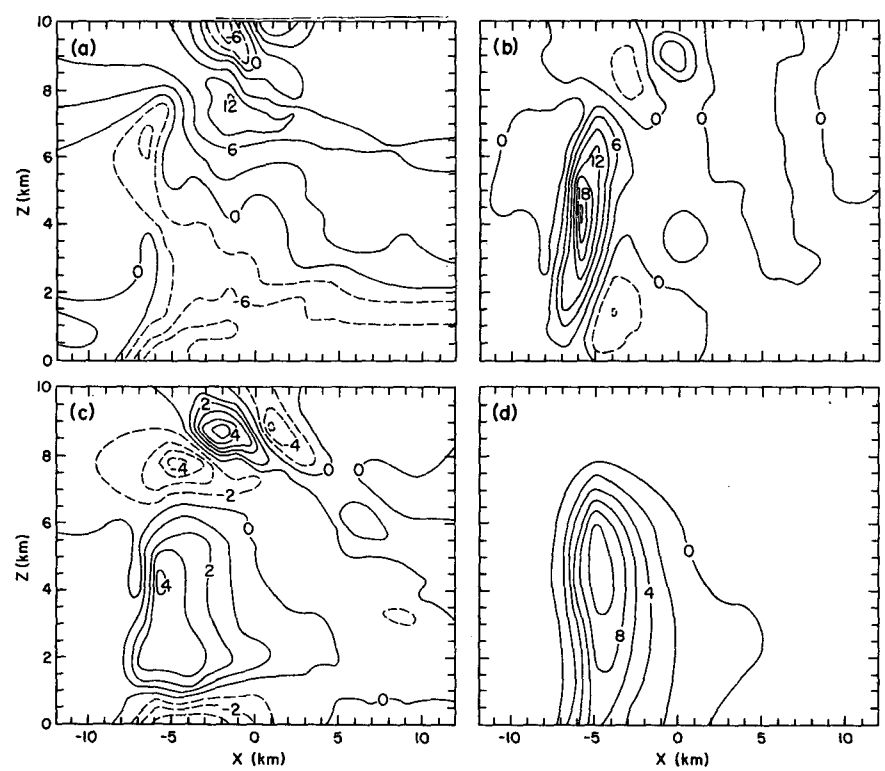

FIG. 5. As in Fig. 4. except at 36 min and (c) $\theta-\bar{\theta}$ field in (°C).

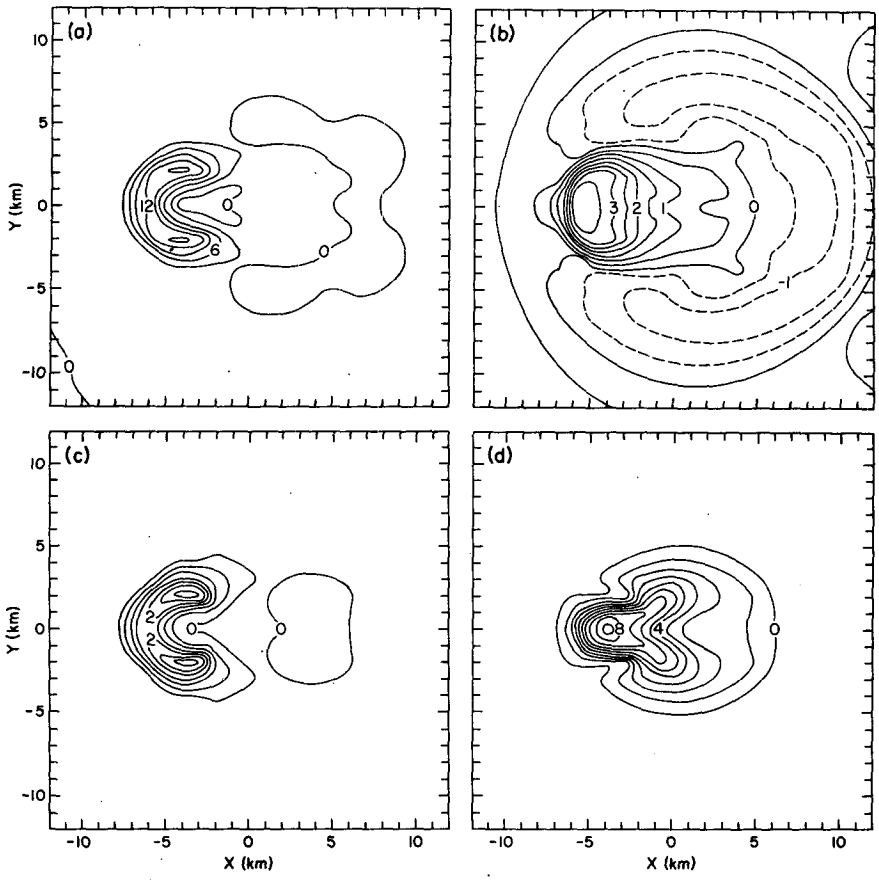

FIG. 6. x-y cross sections at $z=2.75$ km for one-directional shear simulation at 36 min: (a) w field (m s^{-1}), (b) $\theta-\bar{\theta}$ (°C), (c) q_c field (g kg^{-1}), (d) q_r field (g kg^{-1}).

equation in the manner described in Section 2c. For the simulation with the one-directional shear profile given in Fig. 3, the eddy mixing coefficient K_m along the plane of symmetry at $t=24$ min is given in Fig. 7a. Values are largest in the region of strong shear along the upwind side of the cloud and near the top of the cloud where the moist stability is most negative. Converting K_m to turbulence energy via (2.26), the maximum values of E are around 40 m^2 s^{-2} which if divided equally among the three grid velocity perturbations would correspond to u', v', $w'\approx 5$ m s^{-1}. Outside the cloud the ambient stability is sufficient (except near the ground) to maintain Richardson numbers above 0.25 and thus turbulent mixing is suppressed.

Through the analysis of Doppler radar data, Frisch and Strauch (1976) calculated dissipation rates which ranged up to a maximum of about 3600 cm^2 s^{-3} in the region of large horizontal shear of vertical velocity between the updraft and downdraft. For the distribution of K_m shown in Fig. 7a, the maximum dissipation rate [from the last term in (2.21)] corresponds to about 610 cm^2 s^{-3}. Although less than Frisch and Strauch's maximum, this value is reasonable given the intensity of this storm. Undue significance should perhaps not be attached to the exact values of computed turbulence energy until resolution within the model can be improved.

For comparison, the case described above was recomputed using a more conventional mixing coefficient, based only on the deformation of the velocity field (Smagorinsky, 1963). With this approach the mixing coefficient has the form

$$K_m=\frac{c^2l^2}{\sqrt{2}}\left|\frac{\partial u_i}{\partial x_j}+\frac{\partial u_j}{\partial x_i}\right|. \tag{4.6}$$

Deardorff (1972) proposed that for neutral stability one should choose $c=0.14$, while for unstable environments, $c=0.21$ was more appropriate. Using $c=0.21$, the cloud development is similar to that using our formulation at $t=24$ min, although the distribution of K_m as illustrated in Fig. 7b is altered. Since buoyancy effects are not included in the K_m field in Fig. 7b, the overall level of K_m within the cloud is less than that computed from the turbulence energy equation (Fig. 7a). This is particularly noticeable near the ground and the top of the cloud. Steiner (1973) in dry convection simulations found that $c=0.21$ produced insufficient dissipation and that a value of $c=0.42$ led to results which compared more favorably with labora-

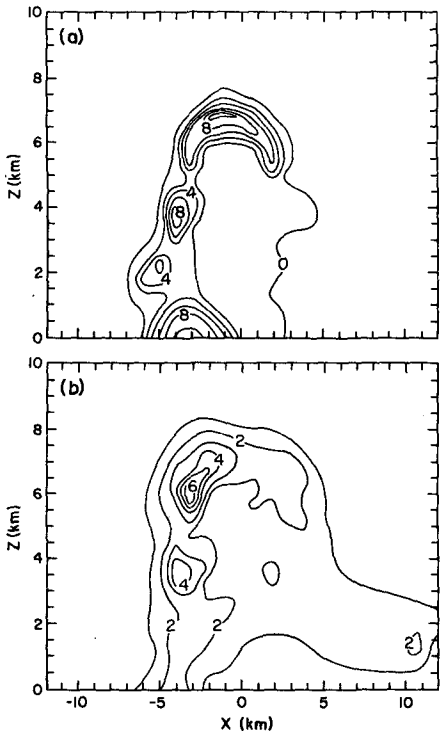

FIG. 7. x-z cross section at $y=0$ for the eddy mixing coefficient ($m^2\ s^{-1}\times10^{-2}$) at 24 min: (a) K_m computed from turbulence energy equation, (b) K_m computed from (4.6) where the contour interval is half that in (a).

tory experiments. He suggested that this larger value of c may be required since feasible grid lengths lie considerably outside the inertial subrange. In our simulation resolution is also rather coarse and a larger value of c appears to be necessary to achieve comparable levels of turbulence energy. Despite the similarity in cloud development we feel that the distribution of turbulent mixing resulting from solving the turbulence energy equation is more consistent with what we would expect from a physical point of view. Further, the effect of including buoyancy in the turbulent energy equation may have a more significant effect for simulations of longer duration.

c. *Evaluation of lateral boundary formulation*

In order to test the performance of our open lateral boundary conditions we utilize a two-dimensional version of the model. With this simplification, we can run a number of variations in the boundary formulation using nominal computer resources and can increase the domain size to provide reference standards for comparison. In many respects two-dimensional simulations provide a more stringent test of boundary conditions than three-dimensional ones since in the former disturbances cannot disperse radially as they propagate outward from the convective region. As a result, perturbations near the boundary tend to be larger in the two-dimensional framework.

For the two-dimensional comparison runs, we specified the grid structure and initialization in the same manner as in the three-dimensional simulations described earlier in this section. Thus the integration domain is 24 km wide and 10 km in the vertical with $\Delta x=1000$ m and $\Delta z=500$ m. The lateral boundary conditions are specified as described in Section 2d with $c_*=30$ m s^{-1}. Temperature and moisture profiles are those depicted in Fig. 1 and the initial perturbation is the two-dimensional form of (4.1) and (4.2). We first consider the case in which there is initially no wind shear present. To illustrate the convection which develops, Fig. 8a displays the contours of horizontal velocity as well as rainwater concentrations in the right

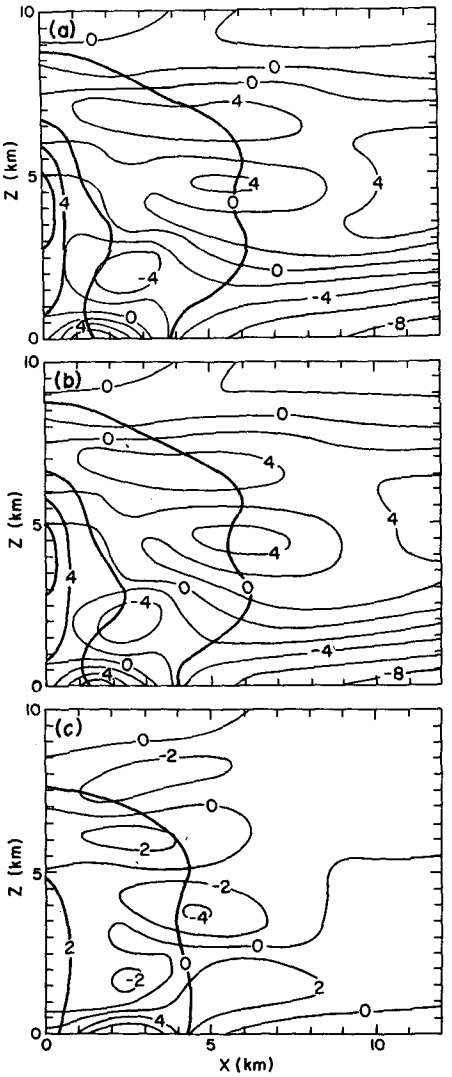

FIG. 8. x-z cross sections of horizontal velocity and rainwater for two-dimensional simulations at 40 min. Light solid lines represent u (m s^{-1}) and heavy solid lines denote q_r (g kg^{-1}). (a) Solution with lateral boundary at $x_L=12$ km, (b) central portion of solution with lateral boundary at $x_L=48$ km, (c) solution with periodic lateral boundary conditions at $x_L=\pm12$ km.

half of the symmetrical domain at $t=40$ min. At this time the updraft is beginning to decay due to the water loading and outflow beneath the cloud has reached 7 m s^{-1} near the ground. Notice also that low-level inflow through the lateral boundary has a maximum intensity of about 9 m s^{-1}.

To provide a reference solution this case was recomputed using the same conditions except that the domain width was increased by a factor of 4. The solution corresponding to Fig. 8a is presented in Fig. 8b and can be viewed as the solution which would result if no lateral boundary were imposed. In Fig. 8b the actual boundary is 36 km to the right of the edge of the figure at $x=12$ km, while in 8a the lateral computational boundary is at $x=12$ km. The two solutions are quite similar and in particular note that the boundary formulation allows strong low-level inflow through the boundary.

For comparison, this solution was also computed using periodic boundary conditions at $x=\pm 12$ km and the results are shown in Fig. 8c. Since no inflow can occur through the periodic boundary, dry descending air outside the cloud cuts off the low-level moisture supply and the convection decays much more rapidly than in the open boundary simulation.

As the integration continues, the low-level outflow progresses outward and reaches $x=12$ km at about 1 h. To demonstrate the ability of the boundary flow to switch from inflow to outflow, we have plotted the horizontal velocity profiles at $x=12$ km at 40 and 80 min for both the small and large domain integrations. The profiles at 40 min correspond to the horizontal velocity at $x=12$ km in Fig. 9a and 9b. By 80 min low-level outflow in the reference case has reached 11 m s^{-1} at $x=12$ km and this structure appears well

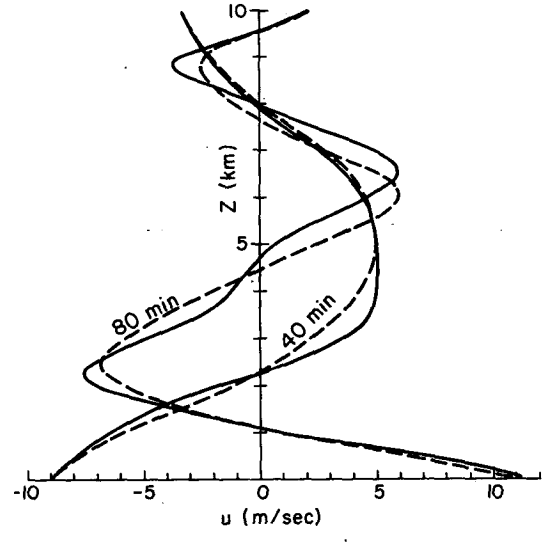

FIG. 9. Horizontal velocity profiles at $x=12$ km for two-dimensional simulations at 40 and 80 min. The solid line is the solution obtained with $x_L=12$ km, the dashed line the reference solution obtained with $x_L=48$ km.

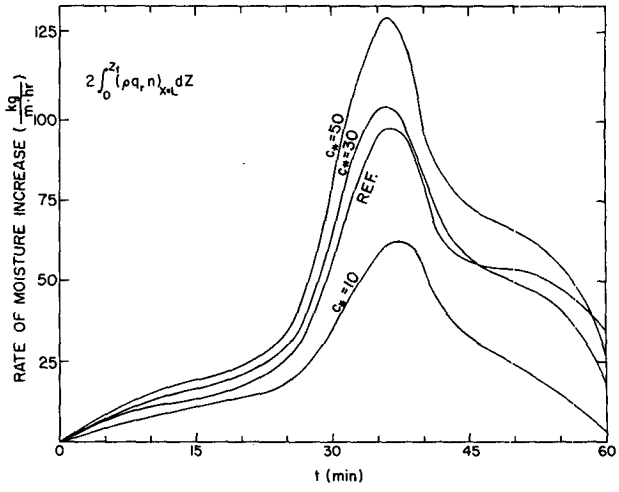

FIG. 10. Net moisture flux through the lateral boundaries for two-dimensional simulations as a function of c_*.

represented in the solution obtained with the boundary located at $x=12$ km.

In Section 2d we mentioned that c_* should correspond to the faster moving internal gravity waves present in the system and that typically $c_*\approx 30$ m s^{-1} is an appropriate value. The solution, however, is somewhat sensitive to the value of c_* chosen in the boundary formulation as illustrated in Fig. 10. Here the net flux of water vapor into the domain through the lateral boundaries is plotted as a function of time for $c_*=10$, 30 and 50 m s^{-1} as well as the flux at $x=12$ km for the reference run generated with a four times larger domain. This moisture flux occurs primarily through low-level inflow and plays an important role in supplying moisture to the cloud. The maximum influx of moisture occurs shortly after the updraft reaches its maximum intensity and eventually becomes negative (shortly after $t=60$ min) when the low-level outflow passes through the boundary. The curves in Fig. 10 demonstrate the sensitivity to the value of c_* and indicate that $c_*=30$ provides good agreement with the reference run. Of course, with periodic boundaries, no net moisture flux can occur through the lateral boundaries.

Some other features of these comparative simulations are presented in Table 1. Here the total rainfall at 1 h represents the mass of rainwater on the ground at one hour per meter in the cross-sectional direction. Although the magnitude of these numbers may not be meaningful, comparing these values among the various runs is informative. The net condensation at one hour consists of the sum of the mass of cloud water, rainwater and rain on the ground. This figure can thus be related to the net latent heat release during that time period. The moisture increase within the domain is obtained by integrating the moisture flux through the boundary over the 1 h time interval (corresponding to the area under the curves in Fig. 10) and relating this result to

TABLE 1. Sensitivity of cloud features to variations in the lateral boundary formulation and in microphysical parameterization.

	Maximum updraft velocity (m s^{-1})	Total rainfall at 1 h (kg m^{-1})	Net condensation at 1 h (kg m^{-1})	Moisture increase in domain (%)	Time for rain to reach ground (min)
		No Shear			
Reference ($c_*=30$, $x_L=48$)	18.5	106	177	46.2	30
$c_*=10$	16.8	71	100	26.7	30
$c_*=30$	18.5	111	178	47.7	30
$c_*=50$	19.1	139	226	58.8	30
Periodic	16.0	38	40	0	30
Periodic ($x_L=24$ km)	17.4	86	110	25.6	30
Microphysical variations					
$a=0$	17.5	119	187	48.3	25
$a=3$ g kg^{-1}	19.4	105	174	48.5	25
Berry autoconversion	19.4	105	174	48.5	34
$V_r+30\%$	18.6	128	185	48.3	26
		10^{-3} s^{-1} *Shear*			
Reference ($c_*=30$, $x_L=48$)	13.7	61	105	31.6	31
$c_*=10$	12.7	37	52	19.3	31
$c_*=30$	14.0	65	112	36.3	31
$c_*=50$	14.5	84	149	44.2	31
Periodic	12.4	22	23	0	31

the total amount of moisture initially present in the domain. The time for rain to reach the ground is arbitrarily defined to be the time at which the maximum accumulation at the ground reaches 0.5 mm.

Comparing these characteristics for the no-shear cases reveals that the solution is significantly influenced by the lateral boundary conditions (see Table 1). This result is not surprising when we observe in the reference run that the moisture contained within the small domain ($|x| \leqslant 12$ km) increases by 46% after 1 h of integration. The solution with $c_*=30$ m s^{-1} produces a similar increase in moisture and compares well with the reference solution in the other characteristics listed in the table. Choosing $c_*=10$ m s^{-1} produces less moisture influx and less condensation, while $c_*=50$ m s^{-1} yields values which are too large. The periodic case would correspond very nearly to $c_*=0$ and differs greatly from the reference case. Although the updraft intensity with $c_*=0$ is not much less than the reference (16 vs 18.5 m s^{-1}), the convection decays much more rapidly; the net condensation at 1 h is only one-quarter as much and almost all of the condensed water has rained out of the atmosphere. Doubling the domain size with periodic boundary conditions yields a solution which is similar to the small domain case with $c_*=10$ m s^{-1}. By further increasing the domain to $x_L=48$ km the influence of the boundary conditions on the solution for $|x|<12$ km is greatly reduced and the periodic run corresponds to the reference case.

To further evaluate the lateral boundary formulations we consider a case in which wind shear is present in the initial environment. The temperature and moisture profiles are the same as in the no-shear case described above and a constant shear of 10^{-3} s^{-1} is imposed across the domain as shown in the heavy solid line in Fig. 11. Low-level flow is initially directed from right to left at about 3 m s^{-1}, while near the top of the domain flow moves in the opposite direction at about 7 m s^{-1}. With this velocity profile the cloud remains nearly stationary in the central portion of the domain. As the cell develops, relative inflow occurs at low levels and the outflow at the left boundary actually switches to inflow. This is illustrated in Fig. 11 in the horizontal velocity profiles at the left and right boundaries ($x=\pm 12$ km) at $t=40$ min. The velocity profiles at $x=\pm 12$ km are also included from the reference run obtained with

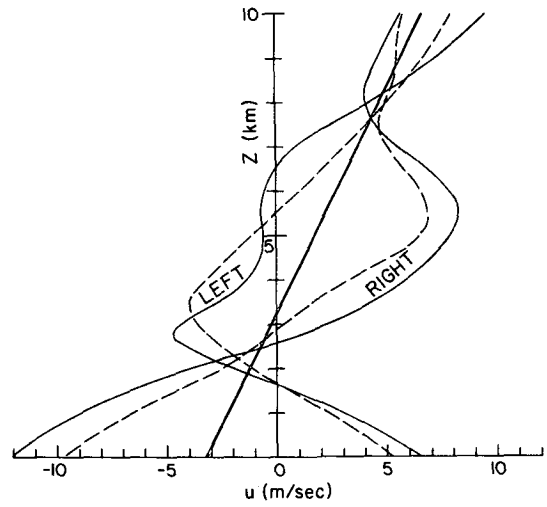

FIG. 11. Horizontal velocity profiles at $x=\pm 12$ km for two-dimensional simulation with linear shear at 40 min. Otherwise as in Fig. 9.

$x_L=48$ km, and exhibit a similar structure to the boundary profiles in the small domain simulation.

Some additional comparisons of the lateral boundary conditions for the shear case are provided in Table 1. These results display a sensitivity to the value of c_* which is similar to that observed in the simulations with no shear. With increasing c_* more moisture enters the domain and greater amounts of condensation occur. The results for $c_*=30$ m s^{-1} compare favorably with the reference simulation although a slightly smaller value of c_* would apparently improve the comparison. Again, with periodic boundaries much less condensation occurs and the fallout of precipitation is almost completed by 1 h.

d. *Some microphysical experiments*

Having provided some indications of the influence of lateral boundary conditions on the accuracy and sensitivity of simulations, it is of interest to consider briefly the corresponding impact caused by certain variations in the microphysical parameterization. Again the two-dimensional framework allows a number of experiments to be economically performed with the results being directly relevant to the three-dimensional situation. For these simulations the model conditions are exactly the same as those used in obtaining the results in Table 1 for the no-shear case with $x_L=12$ km and $c_*=30$ m s^{-1}.

In the expression (2.13a) for autoconversion of cloud water to rainwater, the coefficient a represents a lower bound on the cloud water concentration for the conversion process. For the three-dimensional simulations a is set at 1 g kg^{-1}. To estimate the sensitivity of results to the value of a, characteristics of the simulation are included in Table 1 for $a=0$ and $a=3$ g kg^{-1}. The tabulated figures reflect that increasing a delays the conversion to rain (1 h rainfall is about 12% less for $a=3$ g kg^{-1} than for $a=0$) as well as the time for rain to reach the ground.

Other parameterizations for autoconversion have also been proposed. As an example, we tested Berry's (1968) approach, which has also been analyzed by Liu and Orville (1969) and Murray and Koenig (1972) in two-dimensional models. Liu and Orville found that the Berry formulation inhibited rain formation in the initial stages, but that none of the cases tested produced significantly different dynamical effects. Murray and Koenig also observed that with the Berry parameterization the total rainfall was reduced by about 26% and that the corresponding cloud top height was somewhat less. Although these results are dependent on the actual case being investigated, they illustrate the qualitative influence of this approach.

Using the Berry formulation in our model, the autoconversion with all variables expressed in cgs units has the form

$$A_r=\frac{1.67\times10^4(\bar{\rho}q_c)^2}{5\bar{\rho}+\dfrac{0.0366N_b}{10^6q_cD_b}}, \tag{4.7}$$

where N_b is the particle concentration at cloud base and D_b reflects the relative dispersion of the cloud droplet distribution. Following Simpson and Wiggert (1969) we set $N_b=2000$ cm^{-3} and $D_b=0.146$, which they find to be typical values for continental clouds. Cloud features in this simulation were very similar to those obtained previously by setting $a=3$ g kg^{-1} in the Kessler formulation as indicated in Table 1. Cloud top height, however, was somewhat lower, being about 500 m less than the 8.3 km observed in the other simulations.

As a final experiment, we arbitrarily increased the fall velocity V by 30% over that computed from (2.15). In this case the results in Table 1 show that, as expected, rain reaches the ground sooner and the 1 h rainfall increases by about 15%.

From all of these microphysical variations we find that although quantitative differences arise in the simulations, the results are basically quite similar. In contrast, sensitivity of the solution to changes in the lateral boundary conditions is much more significant, at least for this particular case. Although the influence of the lateral boundaries for equivalent domain dimensions may be reduced in three dimensions, these experiments suggest that special attention should be directed toward the handling of these boundaries.

5. A simulation with a veering and backing wind

The results in the previous section are for simulations initialized with wind shear specified in one direction or with no shear at all. Observations indicate, however, that most storms are embedded in an environmental wind that changes direction with height. For example, in the Great Plains a low-level moisture supply from the Gulf of Mexico capped by dry and sheared air from the west is a favorable sign for storm formation (Palmén and Newton, 1969). Severe continental storms typically occur in environments in which there are significant changes in the direction of low-level winds (e.g., Marwitz, 1972a,b,c). By including a two-directional wind shear in the model, our main purpose here is to demonstrate that the cloud develops a number of interesting characteristics which bear resemblance to observed storm features. More comprehensive analyses of the influence of wind shear will be investigated in a later presentation.

The wind hodograph chosen for the simulation described in this section is shown in Fig. 12. Southerly flow of 10 m s^{-1} veers to westerly flow at 3 km with respect to an assumed origin relative to the ground (⊗). The wind above this level backs rapidly with a

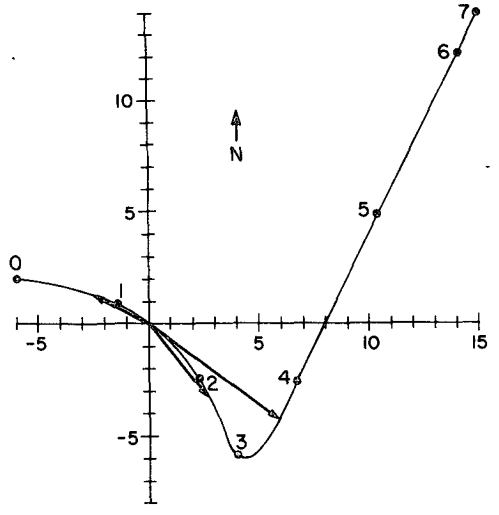

FIG. 12. The environmental hodograph used to initialize the simulation in Section 5. Dots along the curve denote the height (km), velocity labels are in m s^{-1}. ⊗ denotes the absolute origin. The arrows represent the wind vectors at 0.75, 2.25 and 3.75 km.

shear of 8×10^{-3} s^{-1} up to 6.25 km and is then held constant in speed and direction up to 10 km. This hodograph is an idealization of some that exist in the observational literature. For example, it has some similarity to the Grover storm hodograph given by Marwitz (1972a) and to several hodographs for 29–30 April 1970 in Oklahoma documented by Nelson and Barnes (1974) and by Henderson (1974).

The hodograph in Fig. 12 is an extension of one used in a preliminary simulation in which we were investigating how a cloud might respond to veering of low-level winds. In that case the wind veered up to 3.25 km as in Fig. 12, but then was held constant above this level. The results of the simulation were reminiscent of the one-directional shear cases discussed in the last section and the case discussed by Wilhelmson (1974). The similarity occurred because the environmental wind relative to cloud movement was nearly one-directional along a southwest to northeast line. Strong backing and shearing of the wind was added in an attempt to displace the precipitation to the north and east of the updraft and thereby increase the longevity of the storm.

In order to keep the cloud within the central portion of the domain a constant wind component was added to the profile in Fig. 12 such that the wind vectors are taken relative to the origin of the coordinates. The ensuing simulation was then characterized by an updraft which grew to a maximum of 18 m s^{-1} by 24 min. At 28 min a downdraft formed in the lower 2.5 km. As in previous simulations it divided the lower updraft into two parts. The division can be seen at 40 min in Figs. 13a, 13b and 13c which depict horizontal cross sections of the vertical velocity field at 0.5, 2.0 and 3.5 km, respectively. Each relative maximum in the w field is marked in the figures with a C, and the × denotes the locations of maxima in q_r. At 0.5 km the downdraft and the main precipitation region (enclosed by a heavy solid line) occupy the same area while at 2 km the

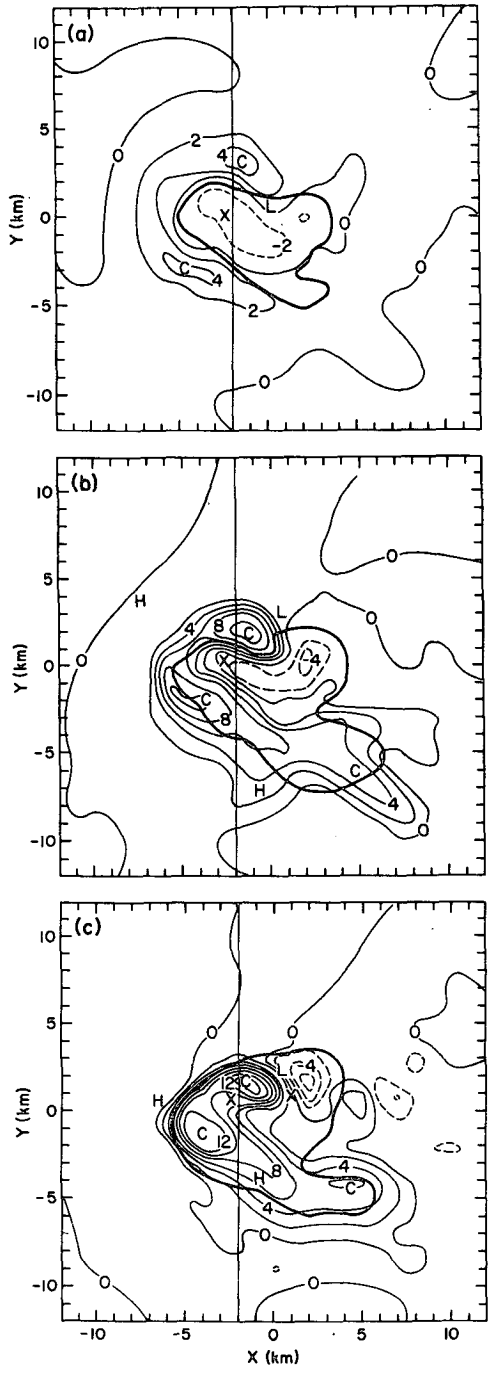

FIG. 13. Horizontal cross sections of w at (a) 0.5, (b) 2.0 and (c) 3.5 km and at 40 min. The q_r field >1 g kg^{-1} is enclosed by the thick line. The × indicates the location of the maximum q_r. H and L indicate the relative pressure highs and lows in the cross section. Maximum relative updraft velocities are marked with a C. The coordinate line at $x=-2$ km indicates the location of the x-z cross sections in Fig. 14.

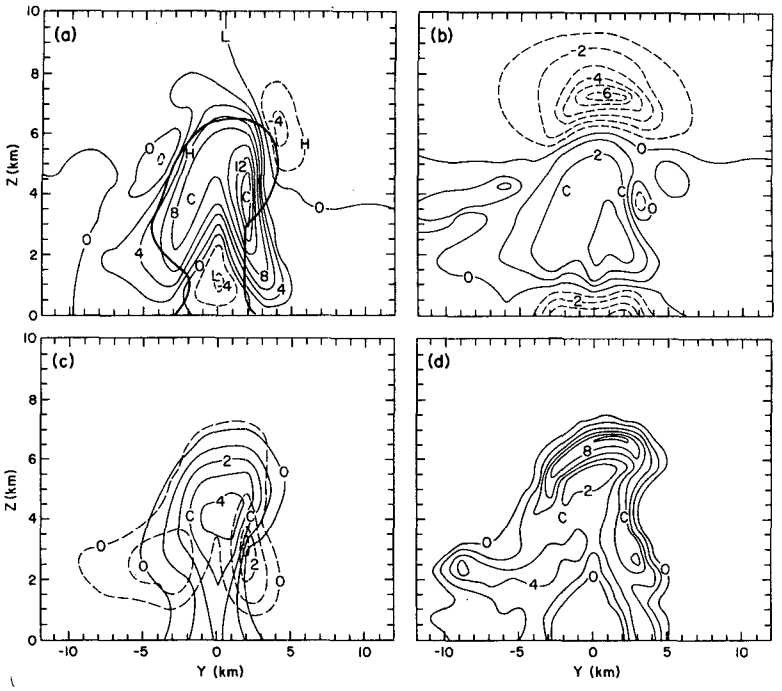

FIG. 14. y-z cross sections at $x=-2.0$ km at 40 min: (a) w field (m s^{-1}) with heavy solid line enclosing the region having $q_r>1$ g kg^{-1}, (b) $\theta'-\bar{\theta}$ field (°C), (c) water fields (g kg^{-1}) where the dash line refers to q_c and the solid line to q_r, (d) K_m field (m^2 s$^{-1}\times 10^{-2}$).

downdraft exists only in the northern part of the precipitation region. On the north and south flanks of the downdraft at 0.5 km there are two updrafts with maximum velocities of 5 m s^{-1}. Two updraft maxima also occur at 2 and 3.5 km. The horizontal plane at 3.5 km passes through the maximum w of 15 m s^{-1} which occurs in the northern updraft. Within this updraft the location of maximum w tilts slightly toward the south in going from 0.5 to 3.5 km. The maximum w in the southern updraft at 3.5 km is 13 m s^{-1} and this updraft tilts slightly toward the north with height. With this structure precipitation falls out between the updrafts as in the one-directional shear simulation (see Fig. 6).

There are several apparent differences between this simulation and this one-directional shear simulation. At 3.5 km a downdraft does occur to the northeast of the northern updraft. However, to the southeast of the southern updraft a secondary updraft has developed which tilts to the northwest with height. This is confirmed in the cloud water field. The secondary updraft continues to increase in intensity until 44 min, the end of the test simulation. Another difference from the one-directional shear case is that two relative maxima in rainwater exist at 3.5 km. One exists in between the updrafts; the other occurs to the east of the northern updraft and the associated water loading apparently enhances the earlier compensating subsidence in this region. The backing of the environmental wind with height thus shifted precipitation to the north and east of the updraft as initially intended. Although splitting of the initial updraft still occurs, the simulation displays interesting features not present in the one-directional shear case as described above.

These features arising in the two-directional shear case do not appear to be related to any spurious influences from the lateral boundaries. An earlier simulation was conducted with the initial u and v components increased by 0.5 and 2.7 m s^{-1}, respectively. Although the cloud moved over to the northern boundary of the domain, the same cloud structure developed as described above. This result provides further verification of the proper behavior of conditions at the lateral boundaries.

Fig. 14 contain y-z cross sections of several fields taken through the location of maximum vertical velocity as indicated by the vertical lines in Fig. 13. Fig. 14 reveals that the two updrafts eventually blend together near the top of the cloud. Cooling occurring near the ground is associated with the downdraft, while that at the top of the cloud is caused by dry adiabatic lifting. Two maxima in cloud water are associated with the two updrafts. The southern one appears weaker because the y-z plane passes to the east of the southern updraft center. A single maximum in the precipitation water field is located above the downdraft. Notice that the lower portion of the northern updraft contains little rainwater, suggesting the formation of an echo-free region or vault on this side of the storm. If the splitting process continues this northern cell would become a left-moving storm. The K_m field

is strongest at the top of the cloud and vanishes in the downdraft region where stability dominates the shear.

The horizontal wind fields at 0.75, 2.25 and 3.75 km are given in Figs. 15a, 15b and 15c, respectively. The relative initial wind vectors at these three levels are indicated in Fig. 12. The lengths of the vectors reflect the wind speed with the distance between adjacent dots corresponding to 5 m s^{-1}. Resolution of the wind fields in Fig. 15 is somewhat coarse since wind vectors are plotted only at every other grid point. Although the cloud does move slowly toward the northwest as determined from the movement of the maximum rainwater near the ground, the vectors shown in Fig. 15 can be taken for practical purposes to be relative to cloud movement. The flow at the boundary is changed from its initial values as the cloud grows and interacts with its environment. After about 25 min patterns of mass and moisture transport into and out of the integration domain are established which persist to the end of the integration at 44 min.

At 0.75 km the flow is inward along all boundaries. Moisture for maintaining the northern and southern updrafts appears to be primarily supplied through the southern and eastern boundaries, respectively. These updrafts are slowly increasing in strength at 40 min and 0.75 km despite the existence of a small negative potential temperature deviation within them. They are rotating as a vortex pair with northern updraft rotating clockwise about its center which is denoted by C and the southern one counterclockwise about its center which is also denoted by C. The downdraft air is nearly coincident with the precipitation region and forms a gust front which is moving primarily toward the west.

At 2.25 km the wind at the boundaries is similar in direction and magnitude to the initial wind at this level except in a small region along the western boundary. Air from the northwest slows down as it approaches the cloud and then some of the air passes around the cloud. The increased velocity along the side of the cloud is typical of flow passing around a cylinder. A double vortex is again observed in the two main updrafts. Southeasterly flow occurs in the new updraft to the southeast and is indicative of air at $z=0.75$ rising to this level. At 3.75 km the boundary winds are again similar in direction and magnitude to the initial wind at this level and environmental air is flowing around the cloud as in obstacle flow.

The highs and lows in the pressure deviation π in Figs. 13–15 are indicated by H and L. The differences between the extreme π values in any cross section are below 1.5 mb. Interpretation of the pressure fields has not been attempted except to note that the western highs at 2.25 and 3.75 km appear to be associated with blocking of the environmental wind.

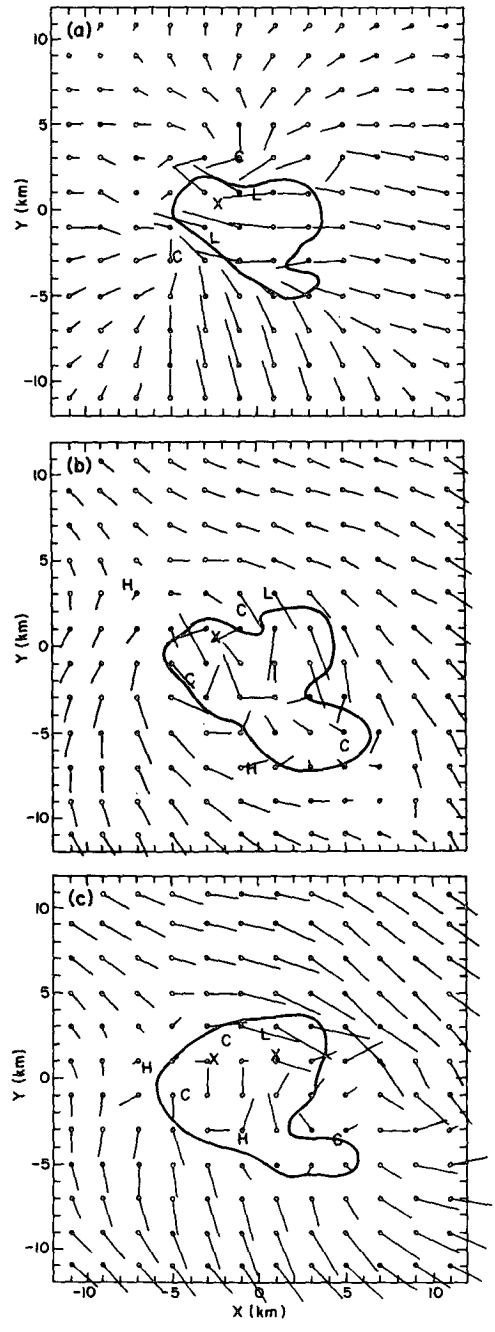

FIG. 15. The horizontal flow field at 40 min with x-y cross sections at (a) 0.75, (b) 2.25 and (c) 3.75 km. The distance between adjacent dots corresponds to 5 m s^{-1} and the undisturbed wind at each level is represented by the arrows in Fig. 12.

6. Summary and discussion

In this investigation we have sought to develop a three-dimensional cloud model which has the ability to simulate the significant features of convective storms. Because of present computational constraints the model is rather crude in its representation of physical processes. However, in spite of this, the model simulations display an encouraging degree of realism and provide a strong justification for continued efforts to document the capabilities and limitations of the model.

Since the numerical procedures and physical parameterizations can have a considerable influence upon the results, care has been taken to use procedures which are appropriate for the present level of sophistication in the model. For the numerical framework we have chosen to solve the compressible equations using a splitting technique which provides computational efficiency by handling the sound wave terms separately with a smaller time step. Since the time-differencing scheme has an explicit form (except for the treatment of vertically propagating sound waves), modifications to the code can be readily incorporated with little impact on the numerical efficiency. For example, although the model does not presently contain a variable surface terrain, this feature could be included using a vertical coordinate transformation and this would only require the addition of scaling factors which would not significantly complicate the computation procedure. For the spatial derivatives, phase errors are reduced through fourth-order differencing of the horizontal advection terms. In practice we find that these fourth-order terms provide significant improvements only when the environmental winds in a simulation are quite strong. Second-order differences are used for all other derivatives.

In representing the microphysics using a Kessler parameterization the impact of rain processes on the model simulations appears to be at least qualitatively correct. Presently the dynamics are strongly influenced by the negative buoyancy produced by water loading as well as by the release of latent heat. Thus it is clear that improving the physics to more accurately represent the distribution of water would be highly beneficial. Unfortunately, such improvements are not easily obtained. In considering the use of individual size categories for drops, a study by Silverman and Glass (1973) indicates that a rather large number of categories must be used in order to achieve better results than provided by the Kessler parameterization. This approach would require large increases in computer time and storage. Furthermore, Clark (1974) emphasizes that in maintaining a parity in the numerical accuracy of dynamical and microphysical processes, a large number of size categories may not be justified if the spatial resolution is too coarse. However, we intend to further investigate the possibility of using a limited number of drop categories because the results of Silverman and Glass were probably influenced by the numerical spreading known to be associated with the use of the Kovetz–Olund technique for coalescence (Soong, 1974) and because Soong (private communication) has had some success in reducing the number of drop categories from 36 to 9 categories for continental clouds. Another approach is being investigated by Clark (1976) who has been developing a microphysical parameterization for warm rain processes using log-normal distributions to represent the drop spectrum. Indications are that this approach will provide improved microphysics at a reasonable computational expense. Besides improving the representation of warm rain processes, we will also seek to investigate the impact of ice and hail development on the dynamics.

The turbulence parameterization developed for the model has a number of attractive features, which include the computation of turbulence energy based on the local buoyancy, shear and dissipation rates, and first-order closure using nearly conservative variables. Although these procedures cannot be rigorously justified for convective storm simulations with coarse resolution, they appear to be appropriate since turbulent mixing is determined by the various physical processes which are considered to be important. In practice, our initial simulations of strong convective storms have not been very sensitive to the detailed distribution of the mixing coefficients because the turbulence energy remains a small fraction of total energy of the storm. Nevertheless, we prefer this approach since the turbulence processes may have a significant influence in longer simulations and also since the required numerical computations are only slightly greater than other simpler techniques.

The fluxes of moisture and momentum through the lateral boundaries exert an important influence on the evolution of simulated storms. As a result, no formulations for these boundaries can be entirely satisfactory. As the cloud dynamics become increasingly dependent on the detailed motion outside the integration domain errors will arise in the simulations. The lateral boundary conditions implemented in the present model help control these errors provided that the cloud does not grow or translate too close to the boundary. Although these boundary conditions are based on very simple theoretical considerations, the two-dimensional simulations in Section 4c document a high degree of realism in representing flow at the boundary.

The model simulations described in Sections 4 and 5 display a number of interesting features which merit further investigation. In the cases with environmental shear the original low-level updraft was split. This splitting appears to be initiated by strong water loading which develops in the central portion of the developing updraft. As the center of the updraft is decelerated, maxima in the vertical velocity develop on either side. Air within these updrafts rotates in the fashion of two counter-rotating vortices. This rotation apparently results from the vertical tilting of horizontal vortex tubes in the inflow region. The updrafts are maintained with low-level moist air flowing normal to the primary direction of the environmental wind, while the rain falls in between the two updrafts. This appears to be a self-sustaining situation. Total splitting of the original cloud may eventually occur with the new clouds propagating away from each other in a manner reminiscent of right- and left-moving storms. In the simulation in Section 5 the low-level southerly environmental flow enhances the moisture supply to the

southern (right-moving) updraft which may result in greater size or longevity of the southern updraft.

Further investigation of the effects of shear on storm maintenance, structure and splitting is currently underway. Observations are being used to help initiate and verify the model to document the value of the model in contributing to the understanding of convective storm dynamics.

Acknowledgments. The authors are indebted to Bill Bergen for his long hours and persistent effort in writing, debugging and modifying model codes during a time in which changes were continually being made to the flow structure and to the numerical model. Thanks also go to Dan Anderson and Jim Ericksen for help in improving the FLOW routines. This research has been supported by the National Science Foundation through the National Center for Atmospheric Research (NCAR) and through Grant ATM 75-19336. The majority of the computation was done using the CDC 7600 at NCAR.

REFERENCES

Asselin, R., 1972: Frequency filter for time integrations. *Mon. Wea. Rev.*, **100**, 487–490.

Beard, K. V., 1977: Terminal velocity and shape of cloud and precipitation drops aloft. *J. Atmos. Sci.* **33**, 857–864.

Berry, E. X, 1968: Modification of the warm rain process. *Preprints 1st Nat. Conf. Weather Modification*, Albany, Amer. Meteor. Soc., 81–88.

Brandes, E. A., 1977: Flow in severe thunderstorms observed by dual-doppler radar. *Mon. Wea. Rev.*, **105**, 113–120.

Browning, K. A., and G. B. Foote, 1976: Airflow and hail growth in supercell storms and some implications for hail suppression. *Quart. J. Roy. Meteor. Soc.*, **102**, 499–533.

Clark, T. L., 1974: A study in cloud phase parameterization using the gamma distribution. *J. Atmos. Sci.*, **31**, 142–155.

——, 1976: Use of log-normal distributions for numerical calculations of condensation and collection. *J. Atmos. Sci.*, **33**, 810–821.

Crowley, W. P., 1968: Numerical advection experiments. *Mon. Wea. Rev.*, **96**, 1–11.

Das, P., 1969: The thermodynamic equation in cumulus dynamics. *J. Atmos. Sci.*, **26**, 399–407.

Davies-Jones, R. P., 1974: Discussion of measurements inside high-speed thunderstorm updrafts. *J. Appl. Meteor.*, **13**, 710–717.

Deardorff, J. W., 1972: Numerical investigation of neutral and unstable planetary boundary layers. *J. Atmos. Sci.*, **29**, 91–115.

——, 1973: The use of subgrid transport equations in a three-dimensional model of atmospheric turbulence. *J. Fluids Eng.*, **95**, 429–438.

——, 1974: Three-dimensional numerical study of the height and mean structure of a heated planetary boundary layer. *Bound.-Layer Meteor.*, **7**, 81–106.

——, 1975: The development of boundary-layer turbulence models for use in studying the severe storm environment. *Proc. SESAME Meeting*, Boulder, NOAA-ERL, 251–264.

Fankhauser, J. C., 1971: Thunderstorm-environment interactions determined from aircraft and radar observations. *Mon. Wea. Rev.*, **99**, 171–192.

Frisch, A. S., and R. B. Strauch, 1976: Doppler radar measurements of turbulent kinetic energy dissipation rates in a northeastern Colorado convective storm. *J. Appl. Meteor.*, **15**, 1012–1017.

Hane, C. E., 1973: The squall line thunderstorm: Numerical experimentation. *J. Atmos. Sci.*, **30**, 1672–1690.

Henderson, J. H., 1974: A detailed description of the internal structure of a thunderstorm. NOAA Tech. Memo. ERL NSSL-69, 111–123.

Hill, G. E., 1974: Factors controlling the size and spacing of cumulus clouds as revealed by numerical experiments. *J. Atmos. Sci.*, **31**, 646–673.

Hoxit, L. R., C. F. Chappell and J. M. Fritsch, 1976: Formation of mesolows or pressure troughs in advance of cumulonimbus clouds. *Mon. Wea. Rev.*, **104**, 1419–1428.

Kessler, E., 1969: *On the Distribution and Continuity of Water Substance in Atmospheric Circulation. Meteor. Monogr.*, No. 32, Amer. Meteor. Soc., 84 pp.

Klemp, J. B., 1978: A splitting procedure for numerical solution of the compressible equations of motion. To be submitted.

——, and D. K. Lilly 1978: Numerical simulation of hydrostatic mountain waves. *J. Atmos. Sci.*, **35**, 78–107.

Kraichnan, R. H., 1976: Eddy viscosity in two and three dimensions. *J. Atmos. Sci.*, **33**, 1521–1536.

Kropfli, R. A., and L. J. Miller, 1976: Kinematic structure and flux quantities in a convective storm from dual-Doppler radar observations. *J. Atmos. Sci.*, **33**, 520–529.

Lhermitte, R. M., and M. Gilet, 1975: Dual-Doppler radar observations and study of sea breeze convective storm development. *J. Appl. Meteor.*, **14**, 1346–1361.

Lilly, D. K., 1965: On the computational stability of numerical solutions of time-dependent non-linear geophysical fluid dynamics problems. *Mon. Wea. Rev.*, **93**, 11–26.

——, 1967: The representation of small-scale turbulence in numerical simulation experiments. *Proc. IBM Sci. Comput. Symp. Environmental Sciences*, White Plains, 195–210.

Liu, J. Y., and H. D. Orville, 1969: Numerical modeling of precipitation and cloud shadow effects on mountain-induced cumuli. *J. Atmos. Sci.*, **26**, 1283–1298.

Marwitz, J. D., 1972a: The structure and motion of severe hailstorms. Part I: Supercell storms. *J. Appl. Meteor.*, **11**, 166–179.

——, 1972b: The structure and motion of severe hailstorms. Part II: Multicell storms. *J. Appl. Meteor.*, **11**, 180–188.

——, 1972c: The structure and motion of severe hailstorms. Part III: Severely sheared storms. *J. Appl. Meteor.*, **11**, 189–201.

Matsuno, T., 1966: False reflection of waves at the boundary due to the use of finite differences. *J. Meteor. Soc. Japan*, **44**, 145–157.

Mellor, G., and T. Yamada, 1974: A hierarchy of turbulence closure models for atmospheric boundary layers. *J. Atmos. Sci.*, **31**, 1791–1806.

Miller, L. J., 1975: Internal airflow of a convective storm from dual-doppler radar measurements. *Pure Appl. Geophys.*, **113**, 765–785.

Miller, M. J., 1974: On the use of pressure as vertical coordinate in modelling convection. *Quart. J. Roy. Meteor. Soc.*, **100**, 155–162.

——, and R. Pearce, 1974: A three-dimensional primitive equation model of cumulonimbus convection. *Quart. J. Roy. Meteor. Soc.*, **100**, 133–154.

Moncrieff, M. W., and M. J. Miller, 1976: The dynamics and simulation of tropical cumulonimbus and squall lines. *Quart. J. Roy. Meteor. Soc.*, **102**, 373–394.

Murray, G. W., and L. R. Koenig, 1972: Numerical experiments on the relation between microphysics and dynamics in cumulus convection. *Mon. Wea. Rev.*, **100**, 717–732.

Nelson, S. P., and S. L. Barnes, 1974: Study of a dissipating severe storm. NOAA Tech. Memo. ERL NSSL-69, 89–96.

Nitta, T., 1964: On the reflective computational wave caused by the outflow boundary condition. *J. Meteor. Soc. Japan*, **42**, 274–276.

Ogura, Y., and J. C. Charney, 1962: A numerical model of thermal convection in the atmosphere. *Proc. Int. Symp. Numerical Weather Prediction*, Tokyo, Meteor. Soc. Japan, 431–451.

——, and N. W. Phillips, 1962: Scale analysis of deep and shallow convection in the atmosphere. *J. Atmos. Sci.*, **19**, 173–179.

——, and T. Takahashi, 1971: Numerical simulation of the life cycle of a thunderstorm cell. *Mon. Wea. Rev.*, **99**, 895–911.

Oliger, J., and S. A. Sundstrom, 1976: Theoretical and practical aspects of some initial-boundary value problems in fluid dynamics. STAN-CS-76-578, Comput. Sci. Dept., Stanford University.

Orville, H. D., and F. J. Kopp, 1977: Numerical simulation of the life history of hailstorms and hail cells. *J. Atmos. Sci.*, **34**, 1596–1618.

Palmén, E., and C. W. Newton, 1969: *Atmospheric Circulation Systems*. Academic Press, 603 pp.

Pastushkov, R. S., 1975: The effects of vertical wind shear on the evolution of convective clouds. *Quart. J. Roy. Meteor. Soc.*, **101**, 281–291.

Ray, P. S., 1976: Vorticity and divergence fields within tornadic storms from dual-doppler observations. *J. Appl. Meteor.*, **15**, 897–890.

——, R. J. Doviak, G. B. Walker, D. Sirmans, J. Carter and B. Bumgarner, 1975: Dual-Doppler observation of a tornadic storm. *J. Appl. Meteor.*, **14**, 1521–1530.

Robert, A. J., 1966: The integration of a low order spectral form of the primitive meteorological equations. *J. Meteor. Soc. Japan*, **44**, 237–245.

Saunders, P. M., 1957: The thermodynamics of saturated air: A contribution to the classical theory. *Quart. J. Roy. Meteor. Soc.*, **83**, 342–350.

Schemm, C. E., and F. Lipps, 1976: Some results from a simplified three-dimensional numerical model of atmospheric turbulence. *J. Atmos. Sci.*, **33**, 1021–1041.

Schlesinger, R. E., 1973a: A numerical model of deep moist convection. Part I: Comparative experiments for variable ambient moisture and wind shear. *J. Atmos. Sci.*, **30**, 835–856.

——, 1973b: A numerical model of deep moist convection. Part II: A prototype experiment and variations upon it. *J. Atmos. Sci.*, **30**, 1374–1391.

——, 1975: A three-dimensional numerical model of an isolated deep convective cloud: preliminary results. *J. Atmos. Sci.*, **32**, 934–957.

Silverman, B. A., and M. Glass, 1973: A numerical simulation of warm cumulus clouds: Part I. Parameterized vs non-parameterized microphysics. *J. Atmos. Sci.*, **30**, 1620–1637.

Simpson, J., and V. Wiggert, 1969: Models of precipitating cumulus towers. *Mon. Wea. Rev.*, **97**, 471–489.

Smagorinsky, J., 1963: General circulation experiments with the primitive equations: 1. The basic experiment. *Mon. Wea. Rev.*, **91**, 99–164.

Sommeria, G., 1976: Three-dimensional simulation of turbulent processes in an undisturbed trade wind boundary layer. *J. Atmos. Sci.*, **33**, 216–241.

Soong, S-T., 1974: Numerical simulation of warm rain development in an axisymmetric cloud model. *J. Atmos. Sci.*, **31**, 1262–1285.

——, and Y. Ogura, 1973: A comparison between axi-symmetric and slab-symmetric cumulus cloud models. *J. Atmos. Sci.*, **30**, 879–893.

Steiner, J. T., 1973: A three-dimensional model of cumulus cloud development. *J. Atmos. Sci.*, **30**, 414–435.

Takeda, T., 1971: Numerical simulation of a precipitating convective cloud: The formation of a "long lasting" cloud. *J. Atmos. Sci.*, **28**, 350–376.

Tapp, M. C., and P. W. White, 1976: A nonhydrostatic mesoscale model. *Quart. J. Roy. Meteor. Soc.*, **102**, 277–296.

Wilhelmson, R. B., 1974: The life cycle of a thunderstorm in three dimensions. *J. Atmos. Sci.*, **31**, 1629–1651.

——, 1977: On the thermodynamic equation for deep convection. *Mon. Wea. Rev.*, **105**, 545–547.

——, and Y. Ogura, 1972: The pressure perturbation and the numerical modeling of a cloud. *J. Atmos. Sci.*, **29**, 1295–1307.

Yamada, T., and G. Mellor, 1975: A simulation of the Wangara atmospheric boundary layer data. *J. Atmos. Sci.*, **32**, 2309–2329.